Geophys. J. Int. (2003) **153,** 443–466

J362D28: a new joint model of compressional and shear velocity in the Earth's mantle

Michael Antolik, Yu J. Gu,* Göran Ekström and Adam M. Dziewonski

Department of Earth and Planetary Sciences, Harvard University, Cambridge, MA 02138, *USA. E-mail: antolik@seismology.harvard.edu*

Accepted 2002 November 12. Received 2002 September 23; in original form 2002 April 5

SUMMARY

The discrimination between chemical and thermal heterogeneity in the Earth's mantle remains one of the most important and challenging questions to be answered by observational and theoretical geophysics. To answer this question requires a thorough knowledge of the ratio between compressional and shear velocity anomalies. We describe results of a joint inversion for compressional and shear velocity in the mantle using a large and diverse data set consisting of traveltimes, complete waveforms and surface wave dispersion measurements. A horizontal tessellation consisting of 362 spherical splines is used to parametrize the model, which is approximately equivalent to a spherical harmonic of degree 18 in resolution. The model contains peak variations (from PREM) of up to ± 7 per cent in S velocity and ± 2.5 per cent in P velocity in the upper mantle. These variations decrease to ± 1.5 and ± 0.6 per cent, respectively, at 1000 km depth and reach ± 2.5 and ± 1.0 per cent, respectively, in the D$''$ region. The rms ratio of S to P velocity perturbations is fairly constant between 2.0 and 2.5 in the lower mantle, but a local minimum in this ratio occurs at a depth of approximately 1700 km. Resolution tests show that the recovery of P and S velocity is not geographically uniform, but also show that this amplitude ratio is well resolved between 670 and 2700 km depth. We also observe a persistent negative correlation between bulk-sound and shear velocity throughout the same region of the mantle. In addition, the model contains a minimum correlation between P and S velocity between 670 and $\sim$1100 km. This feature is supported by both the favourable outcome of resolution experiments and the poor fit provided by the starting model from the inversion (in which the P and S velocities are perfectly correlated) to our data set of P-wave traveltimes. The power spectra of both P and S velocity heterogeneity are similar, although we note a slightly larger dominance of degree two in the spectra for P velocity in the mid-mantle where resolution is highest.

Key words: event location, mantle heterogeneity, seismic velocities, tomography.

1 INTRODUCTION

Improving our knowledge of velocity heterogeneity within the interior of the Earth can have two very important benefits. One of these is that it will lead to an improved understanding of thermal and chemical variations within the mantle and their implications for the geodynamic processes currently operating. There have been a number of recent studies suggesting a change in chemical composition for at least a portion of the lower mantle (e.g. Kellogg *et al.* 1999; van der Hilst & Kárason 1999), or possibly a change in flow patterns around 1000 km depth or so (Kawakatsu & Niu 1996; Forte & Woodward 1997). No evidence for the latter was found by Gu *et al.* (2001). However, Forte & Mitrovica (2001) suggested a change in the length-scale of mantle flow patterns at approximately 2000 km depth, below a localized peak in viscosity. They also estimated chemical heterogeneity at the bottom of the mantle and obtained variations in iron content of the order of ± 1 per cent, although this is critically dependent on a number of thermodynamic and seismic parameters that are not well constrained.

The question of chemical heterogeneity within the lower mantle may be best addressed by studying the relative variation of shear and compressional velocities. Several of the recent models obtained through joint inversion for shear and either compressional or bulk sound velocity show an increase in the ratio $\partial(\ln V_s)/\partial(\ln V_p) = \frac{\delta V_s}{V_s} \Big/ \frac{\delta V_p}{V_p}$ (hereafter called ν) with depth and/or a significant negative correlation between shear and bulk sound velocity for all or some portion of the lower mantle (e.g. Su & Dziewonski 1997; Ishii & Tromp 1999; Masters *et al.* 2000). This may indicate influences on velocity heterogeneity from factors other than thermal structure. To effectively estimate the relative variations of shear

*Now at: Lamont–Doherty Earth Observatory, Columbia University, 61 Route 9W, Palisades, NY 10964, USA.

to compressional velocity with depth throughout the whole mantle requires the simultaneous use of different types of data (i.e. traveltimes of various phases and longer-period data such as surface wave phase velocities or complete seismograms). This is because of the vastly different mantle sampling of these data sets (Gu *et al.* 2001), and is the approach followed in this study.

The second important benefit to be obtained from improved tomographic studies is better knowledge of earthquake locations. This is particularly relevant since the signing of the Comprehensive Nuclear Test Ban Treaty (CTBT) in 1996. The CTBT bans all nuclear tests down to the smallest yields. The major component of verification for this treaty is provided by the International Monitoring System (IMS). Initial locations for seismic events are to be provided by the primary seismographic network of 50 globally distributed three-component stations and arrays. It is a considerable challenge to accurately locate events in the small-magnitude range for which few phase observations are available. A major research effort is currently underway (e.g. Firbas 2000; Group-2 Calibration Consortium 2000; Ryaboy *et al.* 2001) to calibrate the IMS seismic network with station corrections derived from regional and global 3-D velocity models.

Global 3-D velocity models were recently used for location tests by Antolik *et al.* (2001). They tested a number of models with different parametrizations and levels of resolution, and found that although all of the 3-D models improved locations over a 1-D reference model, the most densely parametrized models did not produce the most accurate locations. These tests were carried out using teleseismic *P* waves (25°–96° distance) from a data set of explosions and earthquakes with well-constrained locations. A number of possible reasons were suggested for this result. For example, it was found that the 'higher-resolution' (finely parametrized) models, represented in terms of small constant-velocity blocks, often predicted smaller-amplitude residuals than the 'lower-resolution' (more coarsely parametrized) models for sources located in certain regions. Thus there are indications that longer-wavelength anomalies may not be as well recovered in models based on local parametrization (i.e. blocks) as opposed to globally defined functions such as spherical harmonics. Block parametrizations may achieve better spatial resolution at the expense of some spectral resolution (Chiao & Kuo 2001). Alternatively, this issue may be related to the differing model regularization methods used in tomographic studies (Boschi & Dziewonski 1999).

Another issue relevant to the earthquake location problem is the data used in global tomographic studies. Because of computational limitations most block models have been constructed using traveltime data alone. Many of the 'lower-resolution' models (e.g. Su & Dziewonski 1993, 1997) have made use of data such as surface wave phase and group velocities and normal-mode splitting functions. Only recently have higher-resolution models (equivalent to a degree 18 or higher harmonic expansion), particularly of *P*-wave velocity, been obtained (e.g. Masters *et al.* 2000) using other data in addition to traveltimes. Teleseismic traveltimes have their maximum sensitivity to structure in the lower mantle, whereas other data sets contribute the primary coverage of the region above the 670-km discontinuity (Gu *et al.* 2001). Resolution within this depth range is most critical for the improvement of earthquake locations (Antolik *et al.* 2001). Finally, the extent to which inaccuracies in source locations trade off with structure in seismic tomography is still uncertain. This effect is likely to be largest in the upper mantle. Models containing more free parameters that attempt to fit traveltime data that are less accurate in some regions may result in lower data misfit but be unable to further improve event locations.

In this study we perform a global joint inversion for mantle compressional and shear wave velocity. Our aim is to obtain a medium-resolution model that demonstrably improves event locations for the purpose of providing model-based traveltime corrections to teleseismic phases recorded by the IMS seismic network. In addition we seek an improved understanding of the relative variation of compressional and shear velocities throughout the mantle. We achieve this by inverting a broad range of data sets having sensitivity to mantle structure at different depths. At the top of the upper mantle and in the lowermost ∼250 km, however, the smaller data sensitivity to compressional velocity variations inhibits reliable recovery of the ratio of shear to compressional velocity anomalies. In the discussion that follows, we concentrate mainly on the compressional velocity model since relatively fewer such models have yet been published. We perform earthquake location tests using the new *P*-velocity model to compare its performance against other recent models.

2 DATA AND METHODS

The procedure that we follow is similar to that outlined in Gu *et al.* (2001) and will only briefly be outlined here. For both the compressional and shear velocity models, the perturbations to the reference 1-D model (PREM, Dziewonski & Anderson 1981) are represented by

$$\frac{\delta v(r,\theta,\phi)}{v_\circ} = \sum_{i,j} C_{ij} S_j(\theta,\phi) B_i(r), \tag{1}$$

where the C_{ij} are the unknown model coefficients to be determined, S_j is a spherical B spline as defined in Wang & Dahlen (1995) and in Gu *et al.* (2001), and $B_i(r)$ is a radial cubic B spline. The radial parametrization is the same as that used in the discontinuous model derived by Gu *et al.* (2001) (i.e. 14 radial splines with densest spacing in the upper mantle). The horizontal tessellation and the radial B-spline configuration are shown in Fig. 1. There are a total of 362 spherical spline knots at each radial spline node, making a total number of unknown coefficients of $2 \times 14 \times 362 = 10\,136$. This expansion has approximately the same horizontal resolution as that of a spherical harmonic representation up to degree 18.

The spherical spline representation has a number of advantages over other commonly used parametrizations, such as the 'smoothness' of the model over large distances allowing easier computation of ray paths and traveltimes. In addition, the use of local basis functions means that the resulting kernel matrices will be sparse and can be easily stored and that calculation of the forward problem can be performed very rapidly and efficiently.

2.1 Data sets

In this study we make use of a variety of data sets that provide sampling over the entire depth range of the mantle. These data sets consist of absolute and differential traveltimes, surface wave dispersion measurements, and long-period mantle and body wave seismograms. The upper-mantle portion of the models is primarily constrained by the surface waves and the waveforms, whereas the region below the 670 km discontinuity is primarily constrained by the traveltimes (Gu *et al.* 2001).

We have constructed a new set of global *P*-wave traveltimes for use in this study. This data set consists of ∼626 000 summary rays defined on a 2×2 deg^2 global grid, derived from constituent rays in the distance range between 25° and 100°. Each source is projected to the centre of a block with a thickness of 100 km (except for

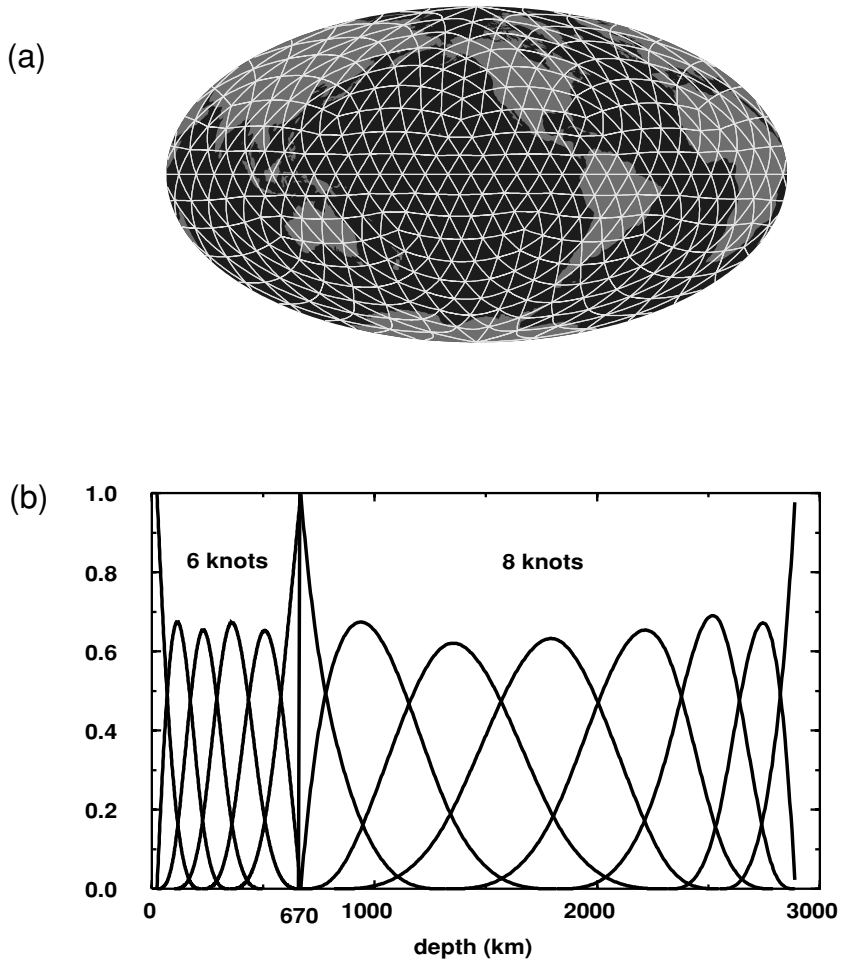

Figure 1. (a) Triangular tessellation used for horizontal parametrization of the velocity model. Spherical spline functions are centred at 362 vertices of approximately equal-area triangles. (b) Radial parametrization of B-splines. There are six basis functions in the upper mantle and eight in the lower mantle. The B-splines are discontinuous across the 670 km discontinuity.

the surface blocks that have a thickness of 50 km). The traveltimes and source locations were first taken from the recompilation by Engdahl *et al.* (1998) of International Seismological Centre (ISC) data. However, since we are not inverting for source locations as part of this study, we account for 3-D structure by first relocating the sources using the model S&P12/WM13 (Su & Dziewonski 1993). This model has previously been demonstrated to significantly reduce the location errors for 'ground-truth' events over 1-D models (Smith & Ekström 1996; Antolik *et al.* 2001). When conducting *P*-wave traveltime tomography, it is particularly important to account for mislocation effects since they can be significant compared with those from velocity variations. Corrections are applied to the summary ray traveltimes to account for ellipticity, station elevation and crustal structure effects (based on Mooney *et al.*'s (1998) global 5×5 deg^2 model CRUST5.1). Fig. 2 shows the coverage (hit count) provided by this data set at three depths within the mantle. The Engdahl *et al.* (1998) compilation includes data for earthquakes occurring between 1964 and 1995. As is typical for such data sets, coverage is generally good for the northern hemisphere (except the north Pacific) but poor for the southern hemisphere and oceans, particularly in the deep mantle. Resolution in the lowermost mantle could be improved by using data from core phases (e.g. *PcP*, *PKP*), but the higher noise level inherent in the ISC data for these phases makes their use more problematic.

The importance of accounting for station (i.e. crustal) and mislocation effects in teleseismic *P*-wave data is shown by Fig. 3. The maps show a comparison of the *P*-wave model of Boschi & Dziewonski (1999) with a model determined from our summary *P*-wave data set. Both models were constructed using the same parametrization (5° equal-area blocks) and damping scheme, and are based only on *P*-wave traveltimes. The difference is that the data used in the former case contained a simpler correction for crustal structure (e.g. Woodhouse & Dziewonski 1984) and were also corrected for source mislocation using an older velocity model (Su *et al.* 1994). The new model contains velocity variations of the order of 0.5 per cent larger in many areas. It is clear that properly accounting for such effects is critical to achieving good resolution throughout the upper mantle. In this case substantial differences are seen down to at least 300 km depth, and could affect conclusions as to the depth extent of velocity anomalies associated with the surface expression of plate tectonics. The differences between the two models decrease with increasing depth.

Because teleseismic *P* waves travel nearly vertically within the upper mantle, adequate coverage is obtained only in the relative proximity of source and station locations. To obtain resolution in other regions of the upper mantle, we employ measurements of surface wave phase velocities and data from long-period seismograms. The surface wave dispersion data were originally collected by Ekström

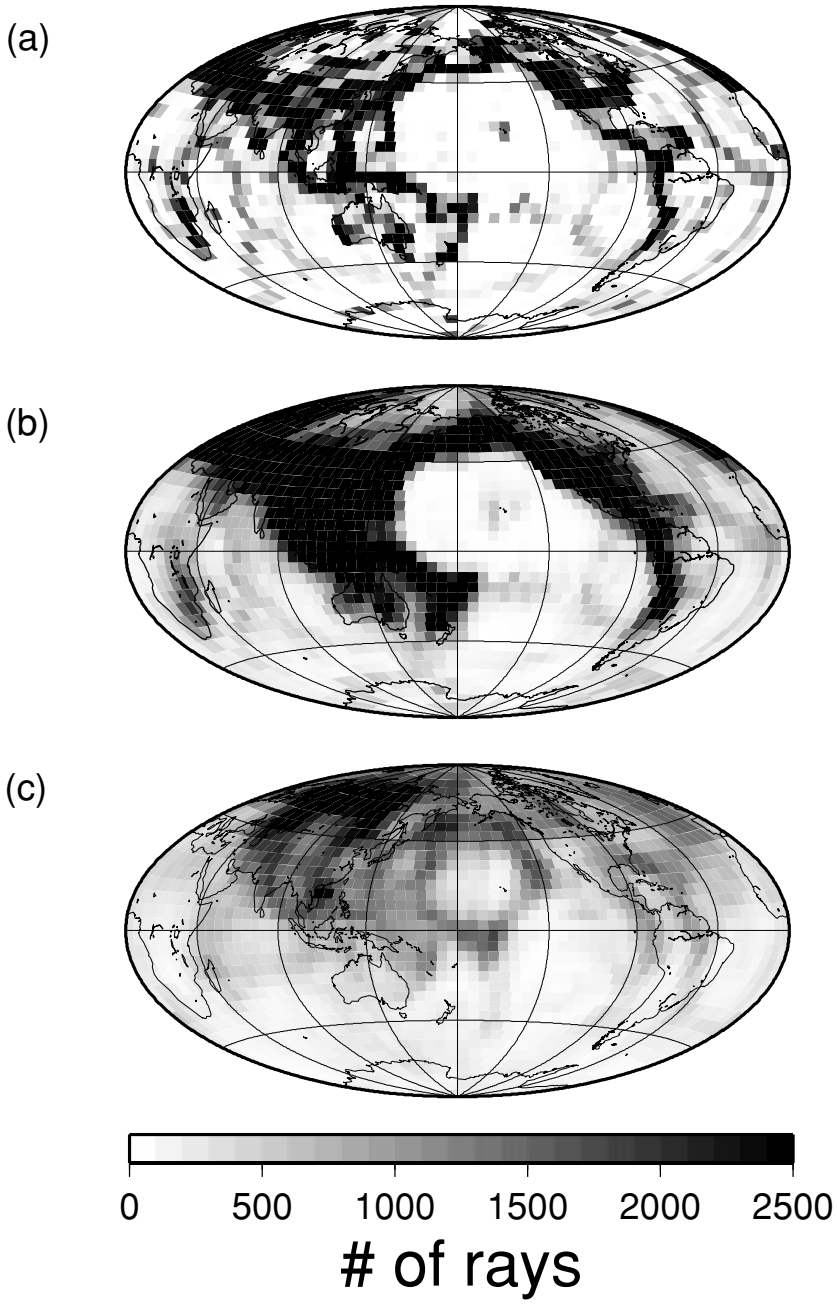

Figure 2. Maps illustrating the number of *P*-wave summary rays in our data set sampling 5 × 5 deg^2 pixels at three depths. (a) Layer ranging from 0 to 193 km depth (beneath the Moho). (b) Depth range 772–865 km. (c) Depth range 2123–2216 km.

et al. (1997) and have been used in the derivation of recent shear velocity models (Ekström & Dziewonski 1998; Gu *et al.* 2001). The data consist of Love and Rayleigh wave phase velocities between periods of 35 and 150 s. Portions of the waveform data have been used in a number of earlier studies (Woodhouse & Dziewonski 1984, 1989; Su & Dziewonski 1993, 1997; Gu *et al.* 2001). The waveform data set includes events recorded between 1977 and 1998 and is separated according to the time period of the events and cut-off period applied (90, 135 and 200 s for mantle waves; 45 s for body waves, see Fig. 4). The synthetic seismograms are computed using mode theory and the path-average approximation outlined in Woodhouse & Dziewonski (1984), although here we correct for phase velocity anomalies affecting the normal-mode eigenfrequencies using Mooney *et al.*'s (1998) crustal model. Although the body wave seismograms contain substantial sensitivity to compressional velocity variations in the upper mantle through the presence of *P*, *PP* and *S*-to-*P* converted phases, the surface wave dispersion data provide little sensitivity to *P* velocity in the upper mantle (because the energy in the fundamental modes is contained largely in shear). We have also included in the inversion a data set of ∼20 000 differential traveltimes of *PP–P* measured from long-period waveforms by Masters *et al.* (2000).

Finally, we make use of long-period absolute and differential traveltimes involving shear phases (Liu & Dziewonski 1998). These include over 40 000 *S*, *SS–S*, *ScS–S*, *S–SKS* and *SKKS–SKS* traveltimes. We do not use short-period *S*-wave traveltimes compiled

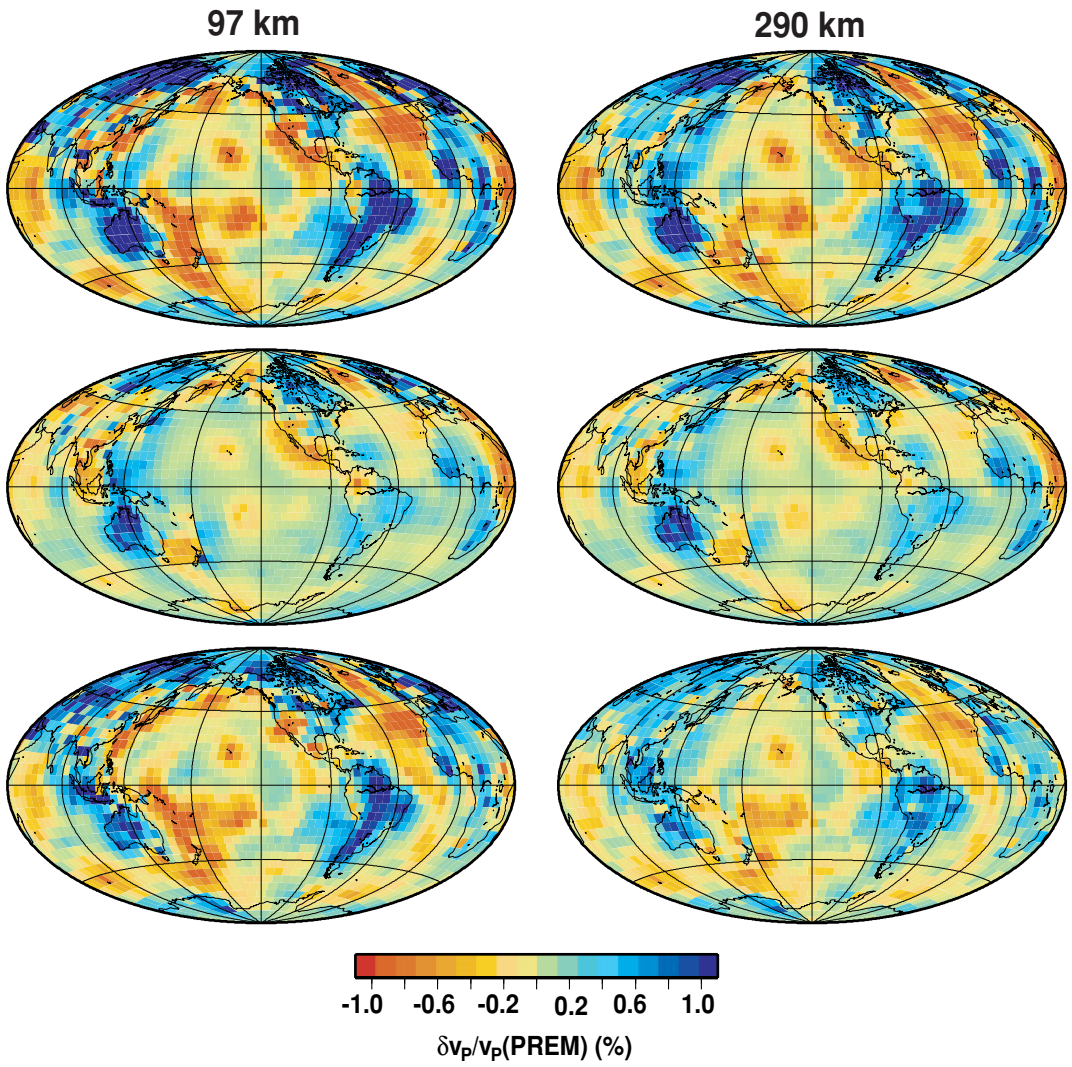

Figure 3. Inversion of summary *P*-wave traveltimes for velocity structure at 97 and 290 km depth. The top two maps show results of inversion for *P* velocity using the improved data set described in the text. The middle two maps show inversion result obtained for data set without improvements by Boschi & Dziewonski (1999). The bottom two maps show the difference between the top and middle results. Inversion with the new data produces upper-mantle anomalies that are not very different in pattern but significantly greater in amplitude.

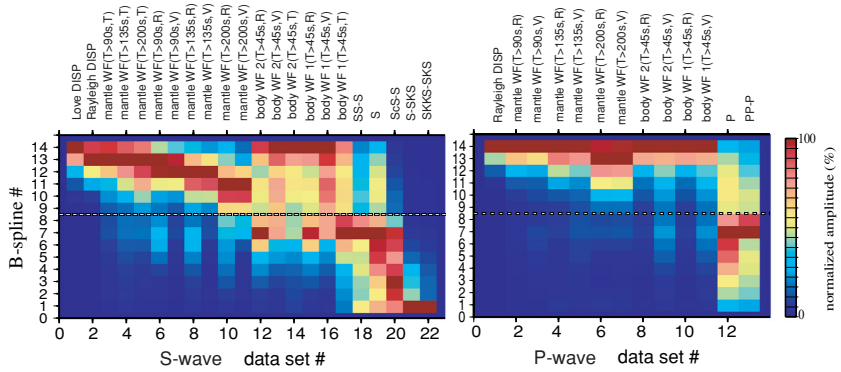

Figure 4. Illustration of the sensitivity of the data sets to structure at various depths in the mantle, represented by the 14 radial spline nodes. The figure on the left shows sensitivity to *S* velocity and that on the right to *P* velocity. The spline functions are numbered in succession from the CMB up to the Moho (refer to Fig. 1 for the depth range covered by each spline). The horizontal dashed line shows the location of the 670 km discontinuity. Each coloured pixel represents the average amplitude of the diagonal elements of the inner product matrix ($\mathbf{A}_T \cdot \mathbf{A}$) corresponding to a particular data set and radial basis function, normalized to the area under that basis function. The amplitude is shown relative to the maximum for each data set. See the text for additional discussion.

by the ISC because of inherent problems with noise and phase misidentification (Robertson & Woodhouse 1995; Masters *et al.* 2000). Since the traveltimes derived from long-period waveforms are subject to bias relative to the shorter-period (∼1 Hz) *P*-wave traveltimes owing to the dispersive effects of attenuation, they are corrected to equivalent 1 Hz times using the PREM *Q* model.

Fig. 4 is an illustration of the sensitivity of each data set to mantle structure at a certain depth for both *P* and *S* velocity, and is analogous to Plate 1c of Gu *et al.* (2001). The numbers on the vertical axes in Fig. 4 represent each of the radial B splines used in the parametrization, ordered from the lower to the upper mantle. Each coloured pixel represents the average of the diagonal elements of the combined inner product ($\mathbf{A}^{\mathrm{T}} \cdot \mathbf{A}$) matrix for a particular data set and radial spline. The value of each pixel is normalized by the maximum value for that data set and corrected for the differences in width of the radial splines (see Fig. 1). Fig. 4 shows the difference in sensitivity to *P* and *S* velocity of the waveform data sets. While uniform resolution in shear velocity is provided by the waveform data sets in the entire upper mantle, their sensitivity to *P* velocity is restricted to just the upper 200 km in depth. In comparison with *S* velocity, a resolution minimum for *P* velocity is indicated by Fig. 4 at the bottom of the upper mantle. This has important implications for the recovery of *P* velocity as will be discussed later. The body wave seismograms also have significant sensitivity to structure around 1000–1500 km depth, but much more so for *S* velocity than *P* velocity. Interestingly the peak in sensitivity for the *PP*–*P* differential traveltimes occurs in the lower mantle near the ray turning depths, despite the fact that each *PP* ray traverses the upper mantle a total of four times.

2.2 Inversion method

We set up the normal equations in the same manner as described in Gu *et al.* (2001), although in this case the inner product matrix is four times larger. However, we deviate from their solution method in terms of the damping applied to the inversion. Because of the differing level of resolution expected in the upper mantle for compressional and shear velocity (i.e. the average of the diagonal elements of the surface wave inner product matrix corresponding to the compressional velocity inversion is roughly 40 times smaller than the corresponding average for the *S*-velocity inversion), we adopt a 3-D target model and invert for perturbations from that model while applying both norm and gradient damping. The target model is the discontinuous shear velocity model derived by Gu *et al.* (2001) (S362D1), scaled by applying the factor of $\nu = 1.82$. At each iteration we seek to solve the matrix equation

$$\delta \mathbf{d}_0 = \mathbf{A}_0 \cdot \delta \mathbf{x}_{3\mathrm{D}}, \tag{2}$$

where $\delta \mathbf{x}^{3\mathrm{D}} = \mathbf{x} - \mathbf{x}_{3\mathrm{D}}$ represents the model perturbations with respect to the target 3-D model, $\delta \mathbf{d}_0$ is the remaining data misfit after the previous iteration and $\mathbf{A}_0$ is the corresponding kernel matrix. To obtain the final solution, we require

$$|\mathbf{A}_0 \delta \mathbf{x}_{3\mathrm{D}} - \delta \mathbf{d}_0|^2 + \lambda_{P,S}^2 |\mathbf{x}_{3\mathrm{D}}|^2 + \eta_{P,S}^2 g^2 = \min, \tag{3}$$

where λ and η are empirically determined constants and g is represented by

$$g^2 = \int_{\Omega} \int_{r_{\mathrm{cmb}}}^{r_{\mathrm{moho}}} |\nabla \mathbf{x}|^2 dr d\Omega. \tag{4}$$

$\mathbf{x}$ in eq. (4) is the total model perturbation with respect to the 1-D reference model (PREM) and the outer integral is over the unit sphere. We require the entire aspherical portion of the model to be smooth, whereas the norm damping is applied only to the perturbations to the target model. The norm damping holds the resulting model solution to be close to the 3-D target model in areas where the resolving power is low (this requirement penalizes solutions where the pattern of compressional velocity variations is dissimilar to that of shear velocity). The constants λ and η are not equal for the *P* and *S* portions of the model. This takes into account the differing sizes of the elements of the inner product matrix. Their values are chosen after performing many inversions and weighing the variance reduction achieved for each data set against the power in the higher degrees of the harmonic spectrum. Because of the smaller resolving power for *P* velocity in the upper mantle, we set the values of λ_P for the six radial splines above the 670 km discontinuity at a factor of 2 larger than for those representing the lower mantle. We found that the final model was relatively insensitive to variations in the damping parameters over a wide range, except for the model amplitudes in depth ranges where resolution is weakest (i.e. near the base of the upper mantle and also just above the core–mantle boundary (CMB)).

For all of the traveltime data sets, we calculate the partial derivative kernels in $\mathbf{A}$ using the ray theory approximation. Although frequency-dependent sensitivity kernels (e.g. Zhou *et al.* 2000) would be more appropriate for the longer-period *S*-wave traveltimes, we use ray theory kernels because the parametrization of our 3-D model is of the same order (the distance between spline knots is ∼1000 km) compared with the Fresnel zones of the waves, and because of the increased computation time that would be required. The kernels for the waveform data sets are computed as described in the previous section.

The total inner product matrix $\mathbf{A}^{\mathrm{T}} \cdot \mathbf{A}$ is obtained through the sum of the contributions from each of the data sets, multiplied by weighting factors that are proportional to the resolving power and inversely proportional to the overall size of each data set. Eq. (3) yields the following full matrix equation relating the model perturbations to the data residuals:

$$\left(\mathbf{A}_0^{\mathrm{T}} \cdot \mathbf{A}_0 + \Pi^{\mathrm{T}} \mathbf{D} + \Lambda\right) \cdot \delta \mathbf{x}_{3\mathrm{D}} = \mathbf{A}_0^{\mathrm{T}} \cdot (\mathbf{d} - \mathbf{A}_0 \cdot \mathbf{x}_{3\mathrm{D}}) - \Pi^{\mathrm{T}} \mathbf{D} \cdot \mathbf{x}_{3\mathrm{D}}, \tag{5}$$

where $\mathbf{x}_{3\mathrm{D}}$ represents the starting 3-D model, Λ is a matrix containing either the value of λ_P or λ_S along the diagonal and zeros elsewhere, Π is a vector containing the constants η_P and η_S mentioned above and $\mathbf{D}$ is the gradient damping matrix defined in eq. (17) of Gu *et al.* (2001). The least-squares solution for $\delta \mathbf{x}_{3\mathrm{D}}$ is obtained using the Cholesky method (Trefethen & Bau 1997), after which we obtain the final model representing perturbations to PREM by

$$\mathbf{x}_{\mathrm{final}} = \delta \mathbf{x}_{3\mathrm{D}} + \mathbf{x}_{3\mathrm{D}}. \tag{6}$$

3 RESULTS

3.1 Shear velocity model

Figs 5 and 6 show the *S* and *P* velocity variations for model J362D28, obtained using $\lambda_P = \lambda_S = \eta_P = 5 \times 10^5$ and $\eta_S = 10^6$ for the lower mantle. For the upper mantle $\lambda_P = 10^6$. The shear velocity model is very similar to the starting model S362D1. All of the major features seen in that model are present in the new model, with some differences in amplitude. The common features in this model and in S362D1 include:

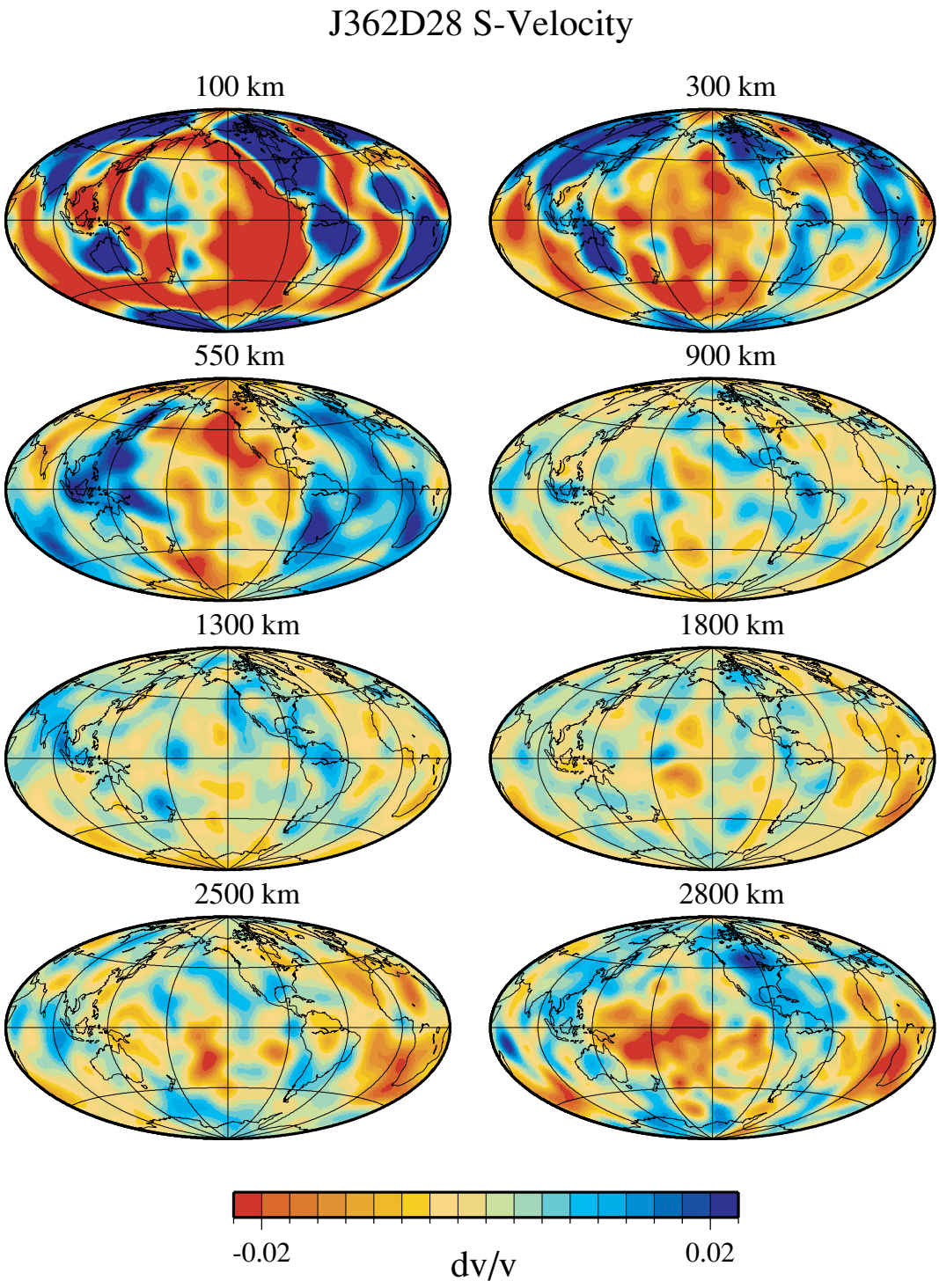

Figure 5. Maps of J362D28 shear velocity variations at eight depths. Colour scale (±2 per cent) is the same for each depth. Maps show velocity perturbations with respect to average structure at that depth.

(1) peak-to-peak variations in shear velocity of over 6 per cent in the upper 300 km related to plate tectonic processes, with large positive variations under shields and platforms and large negative variations under mid-ocean ridges and backarc regions;

(2) dominance of high-velocity anomalies in the mid-mantle, particularly under central Asia, the Pacific and the Americas, some of which have previously been associated with ancient subduction (e.g. Grand *et al.* 1997; van der Voo *et al.* 1999);

(3) two large low-velocity regions in the lower ∼500 km of the mantle under the mid-Pacific and Africa/South Atlantic and a ring of high velocities circling the Pacific basin.

The geographic patterns of these anomalies are very consistent between the two models, which is reflected in the correlation coefficient of larger than 0.9 over most of the mantle. Fig. 7 shows the root-mean-square (rms) amplitude of the *S*-velocity model. The shape

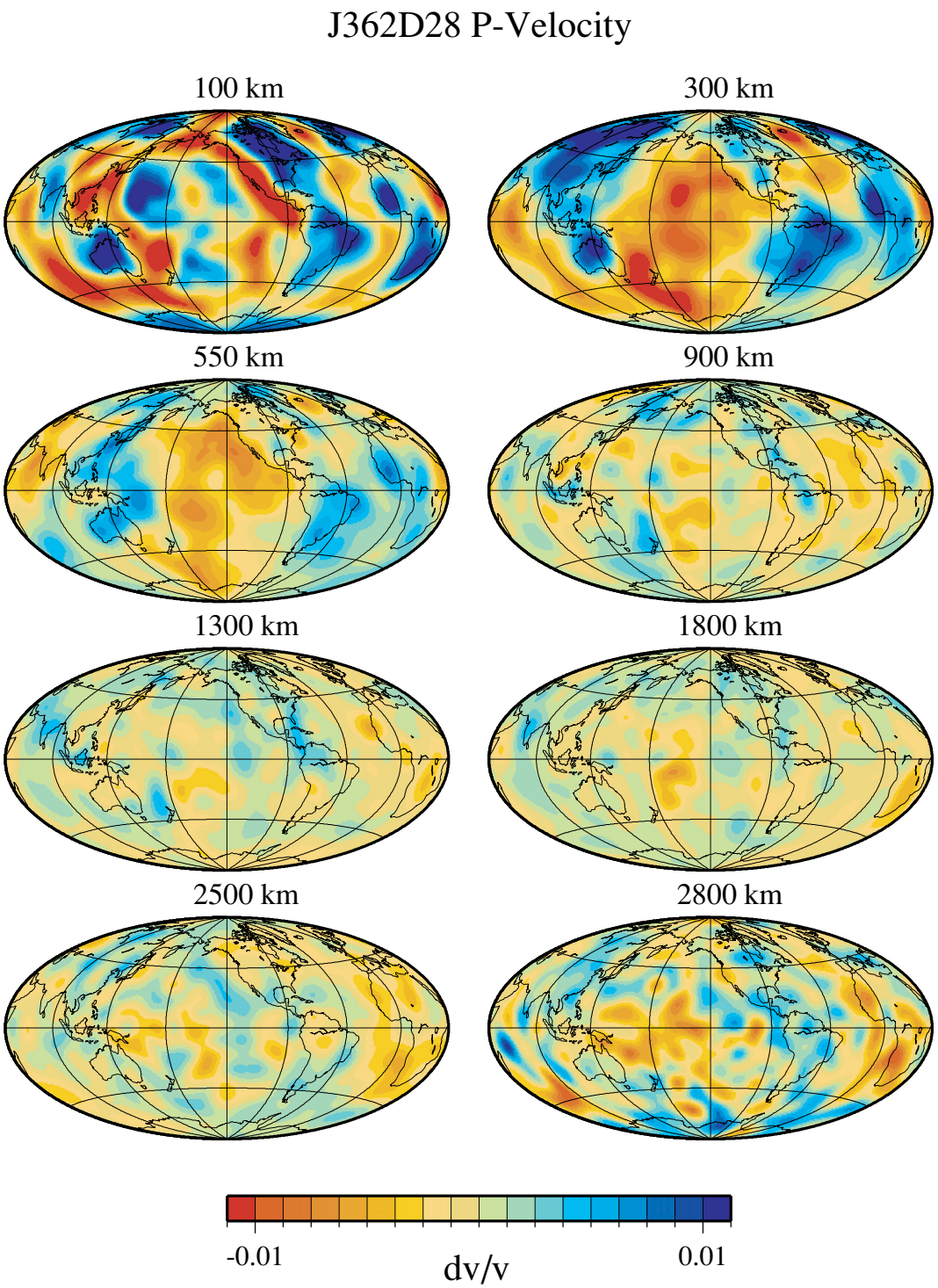

Figure 6. Same as Fig. 5 for compressional velocity. Colour scale (±1 per cent) is again the same for all depths.

of the curve is very similar to that shown in Fig. 10(b) of Gu *et al.* (2001) for S362D1, with the exception of a somewhat higher amplitude at the base of the upper mantle. The average value over most of the lower mantle is around 0.5 per cent, with a minimum occurring at approximately 1500 km. The generally higher amplitude around 500 km depth may be the result of larger damping applied in the earlier study, or it may be related to the improved crustal corrections (from CRUST5.1) that we have applied to the waveform data sets, which comprise a significant proportion of the total data used. The new model provides a better fit to all but one of the waveform data sets used in both studies (Table 1).

3.2 Compressional velocity model

Above 670 km, the *P*-velocity model (Fig. 6) is strongly correlated with that of shear velocity. The maximum variations at 100 km depth

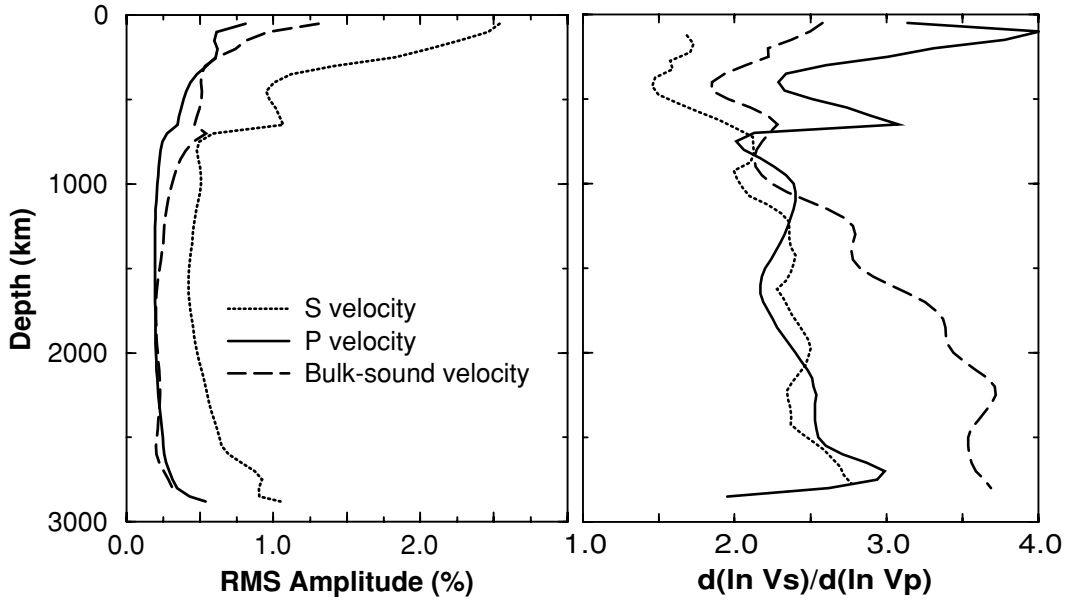

Figure 7. Left: rms amplitude for model J362D28 *P* velocity (solid curve), *S* velocity (dotted curve) and bulk sound velocity (long-dashed curve). Right: value of $\nu = \partial(\ln\ V_s)/\partial(\ln\ V_p)$ in the mantle for model J362D28 (solid curve), model MK12WM13 of Su & Dziewonski (1997) (dashed curve) and model sb10l18 (Masters *et al.* 2000). The ν-value for the current study is very similar to that of sb10l18 in the lower mantle but considerably lower than that of MK12WM13.

Table 1. Variance reduction for traveltime measurements.

Phase	S362D1[a] (%)	J362D28 (%)
P	−6.0	23.8
PP − *P*	32.6	62.9
S	38.9	44.6
ScS[b]	53.8	51.0
SS[b]	33.2	26.8
ScS − *S*	64.6	63.2
S − *SKS*	59.2	66.0
SKKS − *SKS*	25.5	29.0
SS − *S*	72.3	71.7

[a]S362D1 adjusted by constant scaling factor for *P*-wave velocity.
[b]Not used in this study but used in inversion for S362D1.

range from −2 per cent under oceans to +1.5 per cent under continents. These peak variations decrease by a factor of ∼3 down to 550 km. In the mid-mantle there are larger differences between the compressional and shear velocity models. At 900 km, for example, the high-velocity anomaly underlying the eastern Pacific in the *S* model is largely absent in the *P* model. There are some indications of this anomaly present at deeper depths. The long, linear high-velocity anomaly under eastern North America and the Caribbean is quite prominent in the *P* model, with a maximum amplitude of ∼0.5 per cent. A high-velocity anomaly under eastern Siberia also exists in the *P* velocity model but it is absent in the shear velocity model. In the lower half of the mantle, the *P* and *S* models are again extremely similar in the pattern of the anomalies, with the absolute amplitude of the anomalies in compressional velocity being a factor of 2–4 lower. The spatial wavelength of the anomalies in the lower mantle is somewhat smaller for compressional than shear velocity. Low-velocity regions develop in the central and southwest Pacific and under Africa around 1500 km depth and increase in amplitude towards the core–mantle boundary. The ring of high velocities surrounding the Pacific basin is also present to some extent in the *P* velocity model.

The rms amplitude variation in *P* velocity is shown as the solid curve in the left-hand plot of Fig. 7. The amplitude decreases from 0.8 per cent at the top of the mantle to approximately 0.25 per cent through most of the lower mantle. Compared with the *S*-velocity model, the rms amplitude curve is much flatter in the lower mantle and does not begin to increase until approximately 2000 km depth. This feature is also seen in other tomographic models of compressional velocity (Becker & Boschi 2002). However, the rms amplitude of *P* velocity does not increase nearly as quickly towards the top of the model as it does for *S* velocity. This can be seen from a comparison of Fig. 6 with Fig. 5 where the fast cratonic roots are more strongly attenuated in the former. The amplitude of the *P*-velocity model at the top of the mantle is intermediate between other published models (Masters *et al.* 2000; Becker & Boschi 2002), as some have an rms amplitude at the top of the mantle of well over 1 per cent (e.g. Ishii & Tromp 1999), while others have amplitudes as much as a factor of 2 lower (e.g. Fukao *et al.* 2001).

The value of ν ranges between 2.0 and 2.5 for most of the lower mantle, but increases rapidly in the upper mantle (to a peak of ∼4) even though the amplitude of the shear velocity model here is not excessively high compared with other published models (e.g. Vasco & Johnson 1998; Masters *et al.* 2000). ν (Fig. 7) was computed by sampling the models at ∼3000 points at depth intervals of 50 km and taking the ratio of the rms amplitudes. The high value of ν in the upper mantle results mainly from the slower increase in amplitude of the *P* velocity model with decreasing depth mentioned above, and may be an artefact of the lower resolution for *P* velocity compared with *S* velocity (see Section 4). Another secondary peak in ν occurs around 1000 km depth. Some comparisons between shear and compressional velocity models that were not constructed by the same authors show this peak (see Fig. 10 of Becker & Boschi 2002), but it is not seen in previous models obtained by joint inversion (Masters *et al.* 2000). Below a minimum at approximately 1700 km, the ratio increases to approximately 3 at 2700 km depth. Just above the core–mantle boundary ν decreases rapidly. However, as shown in the next section, resolution in the D″ region for *P* velocity is relatively low

compared with that for S velocity. Therefore, the value of v in D″ must be interpreted with caution.

Since we have solved for perturbations in P velocity relative to a starting model that was scaled from a shear velocity model, it is worthwhile to examine how the final P-velocity model differs from this model. Where the pattern of shear and compressional velocities differ, it may point to causes other than thermal variations for these anomalies. Fig. 8 displays this difference ($\delta\ \mathbf{x}_{3D}$) at three depths. Several of the features noted by Ritsema & van Heijst (2002), particularly the slow velocities in the ocean basins at 550 km depth and the prominent lower-mantle high-velocity anomaly under the Pacific and low-velocity anomaly under North America, are also present in Fig. 8. Both regions of slow shear velocity at 2800 km depth (in the central Pacific and Africa/South Atlantic) show faster velocities than expected from the scaled model. Interestingly, the mid-Pacific contains a low-velocity anomaly at shallower depths (1300 km).

3.3 Model correlations

In Fig. 9 we examine the model correlations between compressional, shear and bulk sound velocity. The bulk sound velocity model is computed from the P and S models using eq. (2) of Masters *et al.* (2000). As with many previous joint tomography models, the compressional and shear velocities are highly correlated throughout most of the mantle. In the upper- and lowermost mantle the correlation coefficient ranges between 0.6 and 0.8. The correlation drops sharply across the 670 km boundary and we observe a distinct minimum in the correlation coefficient at the top of the lower mantle. The value remains less than 0.6 until approximately 1200 km depth. Although the sharp drop right across 670 km is a result of the split parametrization in radial basis functions, the lower correlation in the depth range 750–1100 km remains even if we invert for a joint model with a continuous parametrization. This feature has not been noted in previous joint tomographic inversions. Becker & Boschi (2002) have, however, noted that a minimum in correlation between 300 and 700 km depth is a persistent feature in comparisons between existing models of P and S velocity. This feature exists even out to short wavelengths (degree 20 in their comparisons). It is possible that a low correlation in this depth range could be caused by lower resolution of P velocity models relative to S velocity models. The models published by Ishii & Tromp (2001) show a broader, deeper minimum in correlation between P and S velocity centred around 1400 km depth.

As Fig. 9 indicates, the correlation between shear and bulk sound velocity remains negative throughout the mantle, generally ranging between -0.5 and -0.7. Most previous tomographic models do not show a strong correlation between these two parameters at shallow depths in the mantle, although several studies have suggested a strong negative correlation in the lowermost mantle (e.g. Su & Dziewonski 1997; Ishii & Tromp 1999, 2001). The compressional velocity is weakly correlated with the bulk sound velocity, although there is a peak in the correlation that corresponds with the above-mentioned minimum in correlation between P and S velocity. A negative correlation between shear and bulk sound velocity or a decorrelation between compressional and shear velocity have often been cited as evidence for variations in mantle chemistry (e.g. Kennett *et al.* 1998; Masters *et al.* 2000; Forte & Mitrovica 2001). Thus the significance of the depth dependence of correlation between bulk sound, shear and compressional velocity must be investigated through the use of resolution experiments, and we do this in the next section.

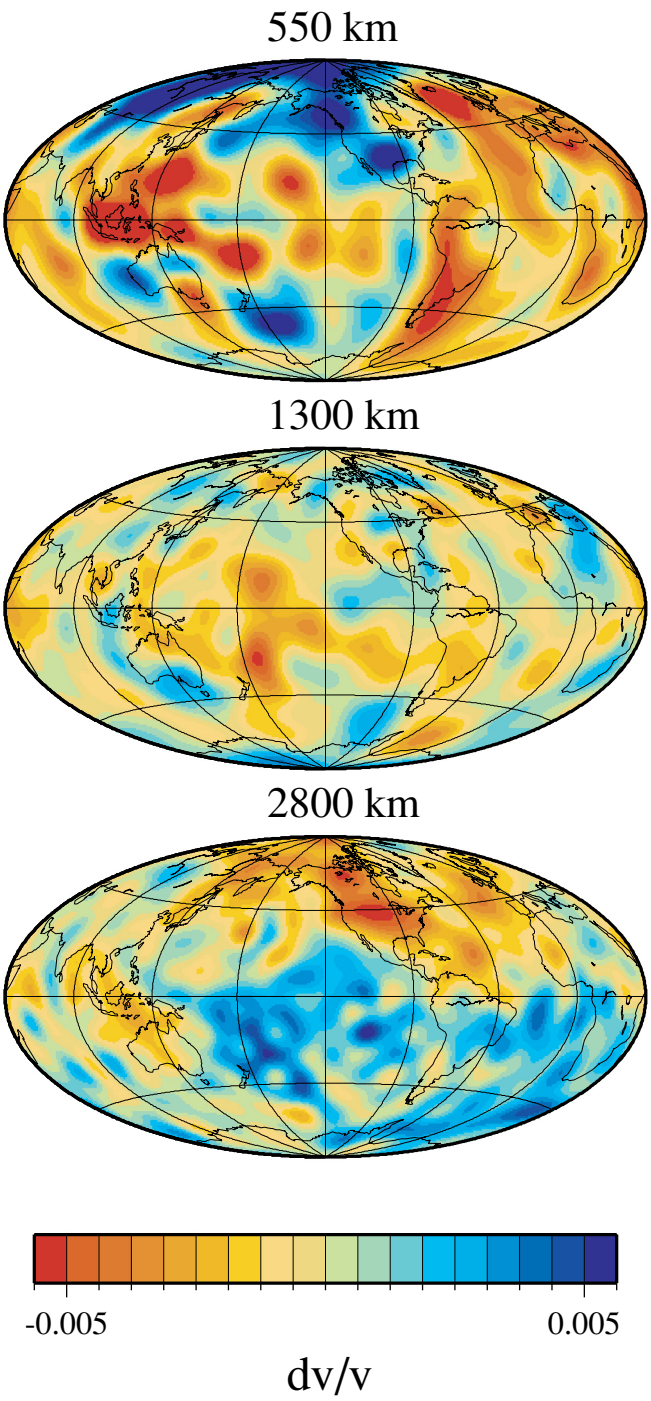

Figure 8. Maps showing the difference of the final P-velocity model from the starting model (modified using the actual scaling factors v obtained by the inversion for each depth, rather than the initial value of 1.82) at depths of 550, 1300 and 2800 km. Areas of large velocity anomalies indicate where the compressional velocity differs from a simple scaled version of the shear velocity.

3.4 Data variance reduction

Tables 1 and 2 show the variance reduction achieved by the new model for the traveltime and waveform data sets and also list that obtained using the starting 3-D model for the inversion. Variance reduction for the kth traveltime data set is calculated as

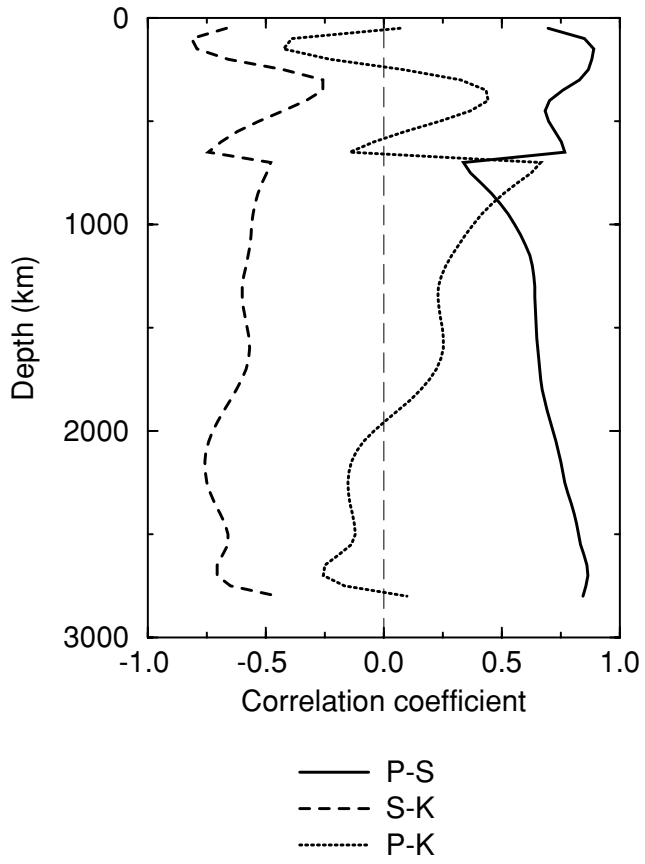

Figure 9. Correlation coefficient versus depth between *P* velocity, *S* velocity and bulk sound velocity (*K*) for model J362D28.

Table 2. Variance reduction for waveform data sets.

Data set	PREM	S362D1 (%)	J362D28 (%)
Body waves set 1[a](V)	35.5	45.5	46.9
Body waves set 1(T)	41.9	51.8	54.2
Body waves set 2[b](V)	36.4	48.3	49.7
Body waves set 2(T)	29.1	37.9	38.7
Body waves set 1(R)	50.3	55.8	57.4
Body waves set 2(R)	44.9	51.5	52.1
Mantle waves, $T > 90$ s (T)	33.3	48.8	55.1
Mantle waves, $T > 90$ s (V)	40.0	63.2	66.1
Mantle waves, $T > 90$ s (R)	32.6	50.3	53.0
Mantle waves, $T > 135$ s (T)	34.5	53.6	60.0
Mantle waves, $T > 135$ s (V)	37.4	58.6	69.9
Mantle waves, $T > 135$ s (R)	48.3	60.4	67.3
Mantle waves, $T > 200$ s (T)	53.6	73.4	75.6
Mantle waves, $T > 200$ s (V)	79.7	84.0	84.5
Mantle waves, $T > 200$ s (R)	74.3	76.4	76.8

[a]Set 1 refers to data with recordings from 1991–1998.
[b]Set 2 refers to data with recordings from 1977–1990.
V, vertical; T, transverse; R, radial; *T*, period. The radial component waveforms were not used by Gu et al. (2001) in their inversion for S362D1.

$$VR_k = 1 - \frac{\sum_{i=1}^{N_k} r_i^2}{\sum_{i=1}^{N_k} r_{i,\mathrm{prem}}^2}, \tag{7}$$

where r_i represents the final residual for the ith datum and $r_{i,\mathrm{prem}}$ is the residual with respect to PREM. The new model achieves similar or higher variance reduction to that obtained using the starting model S362D1 for all of the traveltime data sets that were used in the construction of both models. To some extent this is an expected result since here we employ twice as many free parameters; however, it is not necessarily guaranteed since the shear wave traveltimes have no direct sensitivity to *P* velocity. Approximately 15 per cent greater variance reduction is achieved for the absolute *S*-wave traveltimes and the *SKKS–S* differential traveltimes. The absolute *ScS* and *SS* traveltimes were not used in the present study, yet we still achieve over 50 per cent variance reduction for the former. From Table 1 we can conclude that including the compressional velocity in a joint inversion does not degrade the variance reduction to the shear wave traveltimes.

The total variance reduction for the *P*-wave traveltimes is 24 per cent. For the observations in the distance range 25°–75°, the variance reduction is around 20 per cent and then increases to over 30 per cent between 80° and 95°. For the long-period *PP–P* data set, the final model achieves a variance reduction of over 60 per cent. While we would not expect the starting model to match the variance reduction achieved in this study for the compressional wave data sets, it is somewhat surprising that the values shown in Table 1 are so low. For the differential times, the starting model achieves only half the variance reduction obtained for the final model, and for the direct *P* waves the variance reduction is actually smaller than for PREM. Since the starting model consists of compressional and shear velocity perturbations that are perfectly correlated, this gives an indication as to why we observe relatively low correlation between the final compressional and shear velocity models in the mid-mantle. In contrast, the variance reductions achieved for the mantle waveform and surface wave data sets by the starting and final models are more similar, suggesting higher correlation between *P* and *S* velocities in the upper mantle.

We define the variance reduction for each waveform data set as

$$VR_W = 1 - \frac{\int (u_{\mathrm{obs}} - u_{\mathrm{th}})^2\, dt}{\int u_{\mathrm{obs}}^2\, dt}, \tag{8}$$

where u_{obs} represents the observed seismogram and u_{th} is the corresponding synthetic. As shown in Table 2, the fit to all of the waveform data sets is better for J362D28 than for the starting model. This is true for the transverse component seismograms even though their sensitivity to *P* velocity is negligible. The largest improvement is seen for the intermediate-period data sets (cut-off period of 90 and 135 s). This is most likely a result of very good recovery of long-wavelength anomalies in both models (∼75 per cent variance reduction for the longer-period mantle waves), while a better explanation of the body-wave seismograms requires recovery of smaller-wavelength features beyond the limits of our resolution. In addition, the path-average approximation is less appropriate for the shorter-period waveforms. In Table 2 we have included the CRUST5.1 eigenfrequency corrections for all of the models. This results in a larger variance reduction for all but one of the data sets. The variance reduction obtained for the surface wave phase velocities of different periods is comparable to that reported in Ekström *et al.* (1997) (70–90 per cent).

4 RESOLUTION TESTS

In this section we perform tests using a constant-wavenumber chequerboard pattern to assess which features of the new model described above are real and which are potential artefacts of poor resolution. As demonstrated by Figs 2 and 4, we cannot expect the model resolution to be homogeneous either laterally or with depth, and we should expect poorer resolution for *P* velocity than for *S* velocity. The input model for our experiments consists of a degree-11 chequerboard pattern with maximum velocity perturbations of

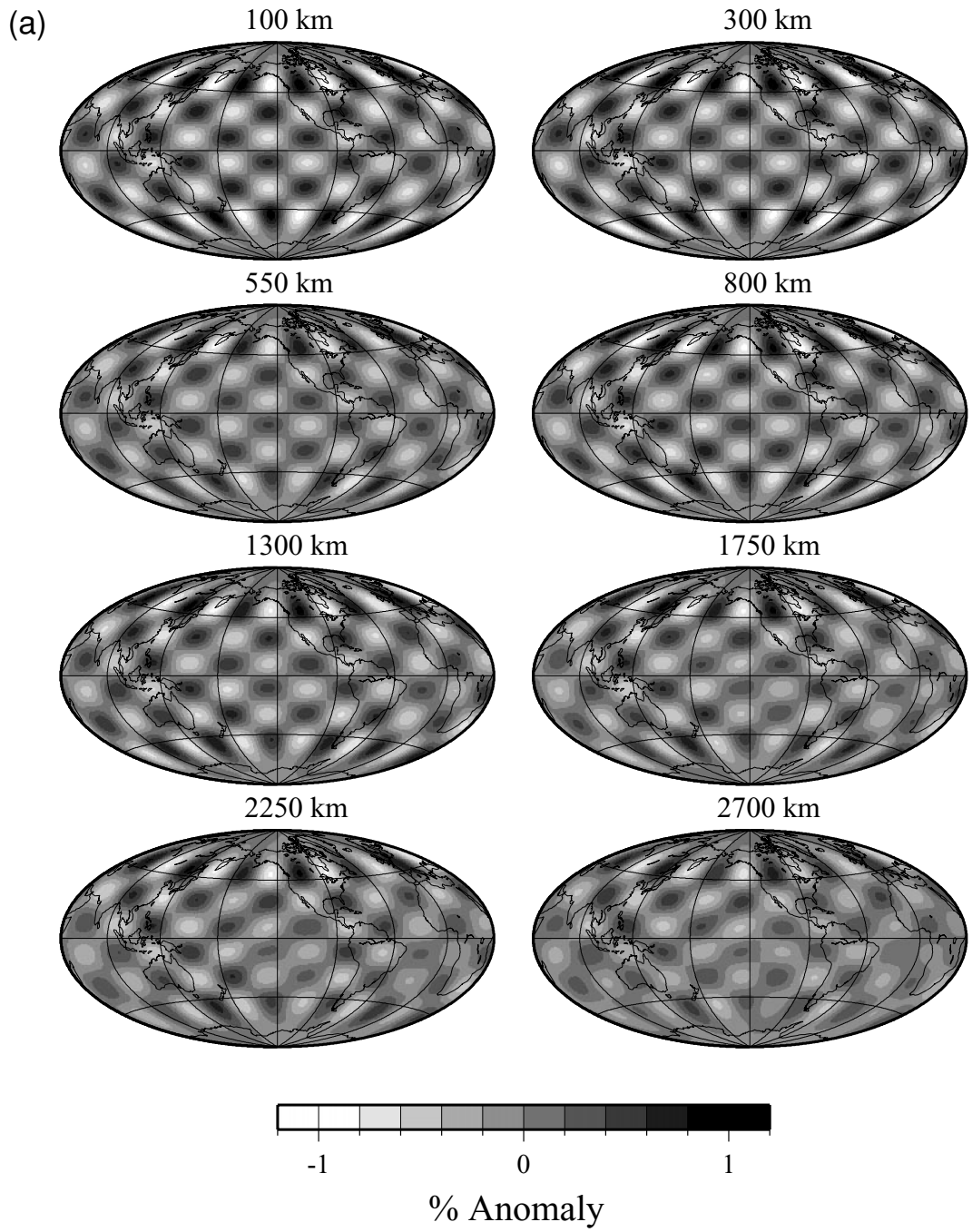

Figure 10. Recovered (a) *S* and (b) *P* velocity models at eight depths for resolution test 1. Input model for this test was null for *P* velocity. Note the much smaller-amplitude scale for (b).

±1 per cent. The input model does not vary with depth. This allows us, for each test, to evaluate the resolution simultaneously at all depths within the model. In the interests of space, we show the results for the degree-11 pattern only. Tests using other input models are displayed at http://www.seismology.harvard.edu. Results of tests using longer-wavelength patterns confirm that the lower degrees are better resolved, and that resolution decreases with increasing harmonic degree. Because of the damping applied, however, the recovered power in degrees larger than 14 is small for both *P* and *S* velocity. The principal conclusions of this study are therefore unlikely to be biased by insufficient resolution at higher degrees.

For each test, we use all of the data sets used in the inversions, the same weighting for each data set, and the same damping coefficients as those used to obtain the final model. Sources and receivers are the same for which we have data. We describe the results of four experiments.

(1) We use the degree-11 chequerboard pattern as the input model for *S* velocity. A null model (zero perturbations to PREM) is input

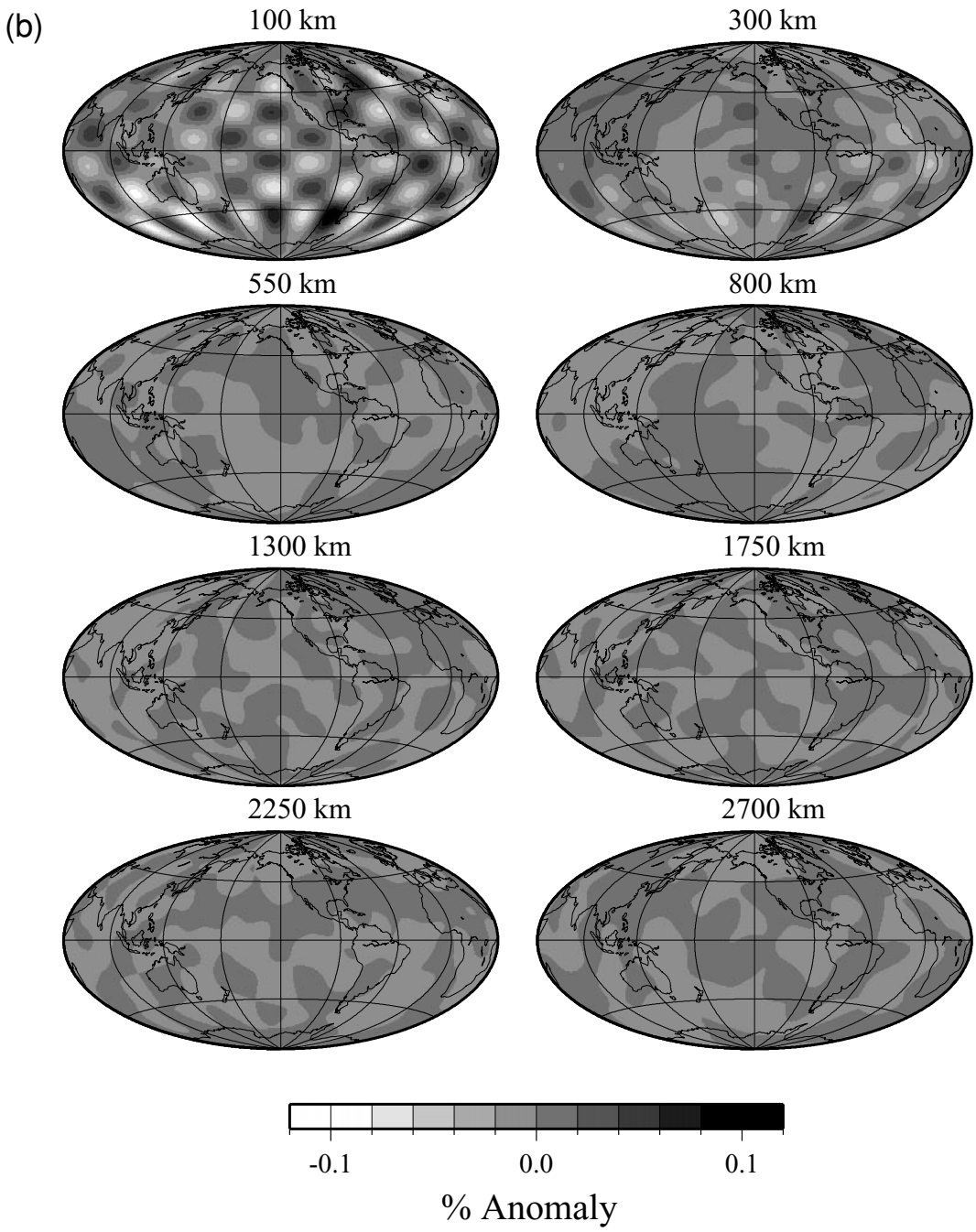

Figure 10. (*Continued.*)

for *P* velocity. This allows us to examine the potential for erroneous mapping of shear velocity perturbations into the compressional velocity model.

(2) The opposite of test 1 where we use a null model for *S* velocity and a chequerboard pattern for *P* velocity.

(3) We use the chequerboard pattern as the input for both *P* and *S* velocity. The two models are scaled by $\nu = 1.82$.

(4) This test is designed to examine the ability to detect sharp changes in heterogeneity patterns across the 670 km discontinuity. For both *P* and *S* velocity, we use a model identical in pattern to the previous tests for the entire upper mantle. At 670 km, the amplitude of both input models drops abruptly to zero and remains so throughout the lower mantle.

Figs 10 and 11 show the recovered models from tests 1 and 2. The input shear velocity model is very well recovered, with a decrease in amplitude below 2000 km depth and also some smearing of anomalies in the lower mantle. Not surprisingly, this effect is more pronounced in the southern hemisphere, even though the degree-11 pattern is still well recovered there. There is little mapping of the shear velocity anomalies into compressional velocity (Fig. 10b), except for the upper 250 km. Below this depth, the recovered anomaly pattern in *P* velocity is essentially random and the amplitude is extremely small (the maximum anomaly is ∼0.01 per cent). Fig. 12(a)

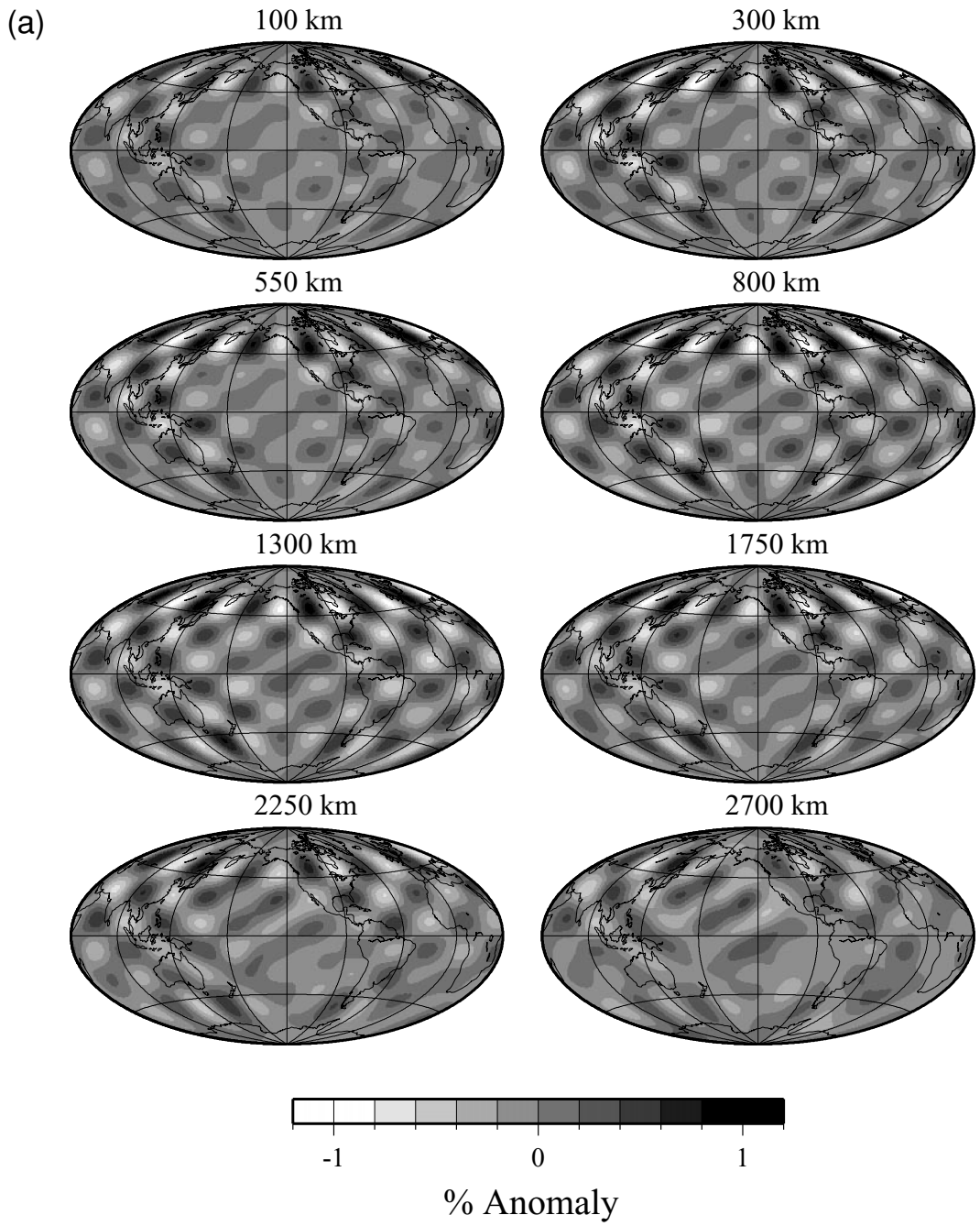

Figure 11. Recovered (a) *P* and (b) *S* velocity models at eight depths for resolution test 2. Input model for this test was null for *S* velocity. Note the much smaller-amplitude scale for (b).

shows that at least 70 per cent of the amplitude of the input shear velocity model is recovered through most of the mantle. Exceptions occur below 2500 km depth and in the immediate vicinity of the 670 km discontinuity. A minimum in resolution, which is more serious for *P* velocity than for *S* velocity, occurs around 670 km because this region lies between the sensitivity maximum for the waveform and traveltime data sets. To improve this situation, dispersion measurements from very long-period surface waves (>200 s period) are needed (Nettles *et al.* 2000). This loss of amplitude is extremely localized, as the recovered model returns to 75 per cent of the input by 700 km depth. Fig. 12(a) also shows that the maximum amplitude anomaly mapped into *P* velocity is 0.1 per cent or 10 per cent of the input pattern.

As expected, the results of the second test show that resolution for *P* velocity is not quite as good as for *S* velocity. The reduction in recovered amplitude in the lower-mantle parallels that for *S* velocity, but a rapid fall-off occurs below 2500 km depth, such that less than 40 per cent of the amplitude is obtained at the core–mantle boundary. As in the *S* velocity case, the peak in amplitude recovery occurs at around 1000 km but is slightly smaller in amplitude. The maximum recovered anomaly amplitude is 70 per cent of the input around 400 km depth, but is less than 40 per cent at the top of the

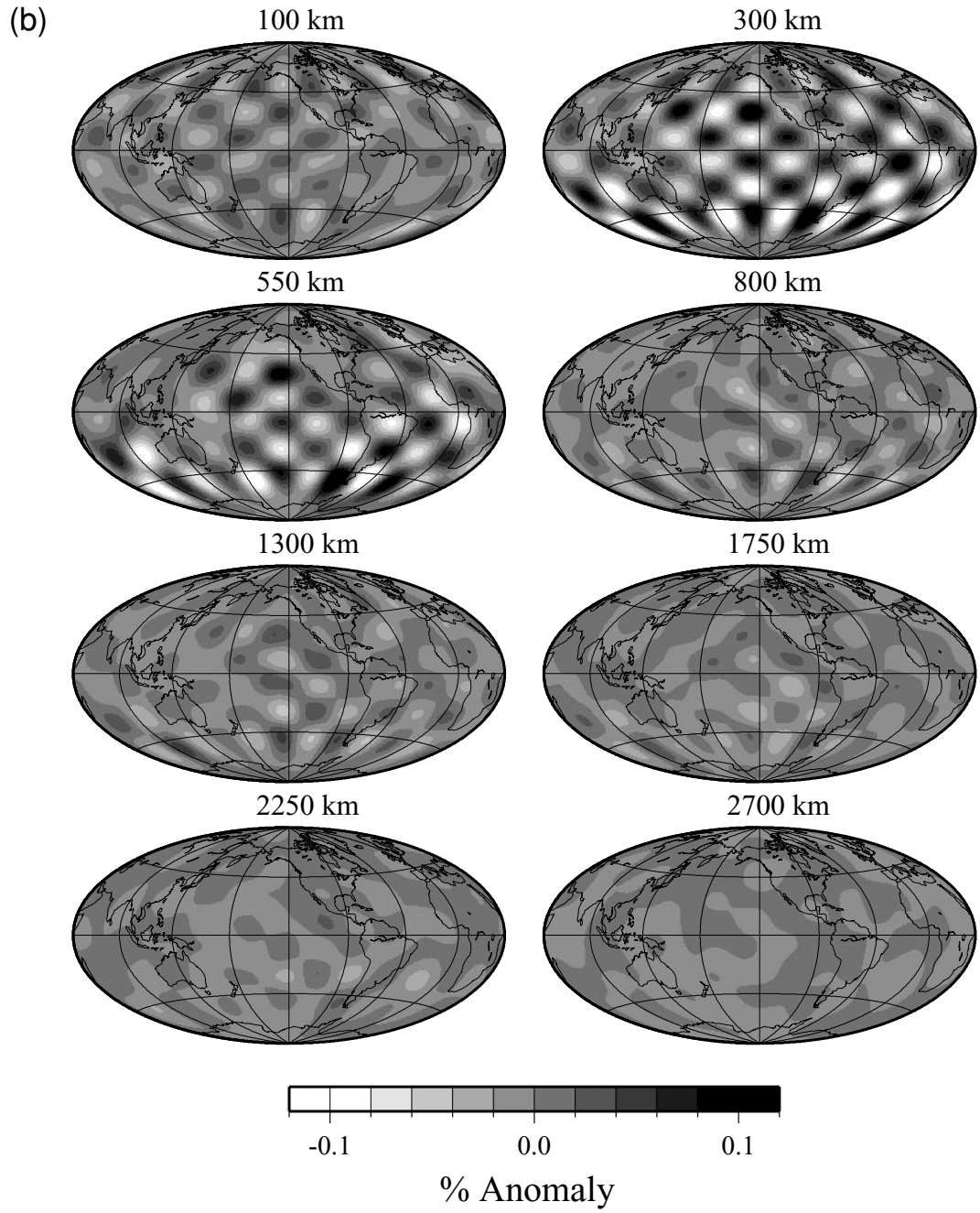

Figure 11. (*Continued.*)

model. Likewise, the drop-off in correlation between the input and output *P* velocity models is more pronounced than for the shear velocity case (Fig. 13), reaching a minimum of around 0.6. Smearing of anomalies also occurs to a larger degree. We note that resolution in the southern hemisphere lower mantle is poor, particularly in the eastern Pacific and under Africa. In the upper mantle, resolution is weak in the central Pacific. However, in the mid-mantle the quality of the recovered compressional velocity model approaches that for *S* velocity. Mapping of compressional velocity anomalies into shear velocity occurs mostly between 200 and 600 km and has a slightly larger amplitude than for the opposite case (Fig. 12b). This is because the peak in sensitivity to shear velocity of the waveform data sets occurs in this depth range. Because the waveform data sets are more sensitive to shear than compressional velocity, the tradeoff is more severe. Very minor amplitude anomalies are mapped into shear velocity in the mid-mantle.

Results from test 3 lead to similar conclusions. Here the input *P* and *S* velocity models consist of the same patterns (scaled by $\nu = 1.8$). The relative amplitude curves for the output models are very similar to those in the previous cases. Model correlations for this test are shown in Fig. 13(c). In this case the input *P* and *S* models are perfectly correlated everywhere in the mantle. The correlation between the output *P* and *S* models is greater than 0.9 everywhere above 2500 km and reaches a maximum around 1100 km. Below this, the correlation decreases to 0.7 just above the CMB. The significance of this result is that we observe no minimum in correlation between

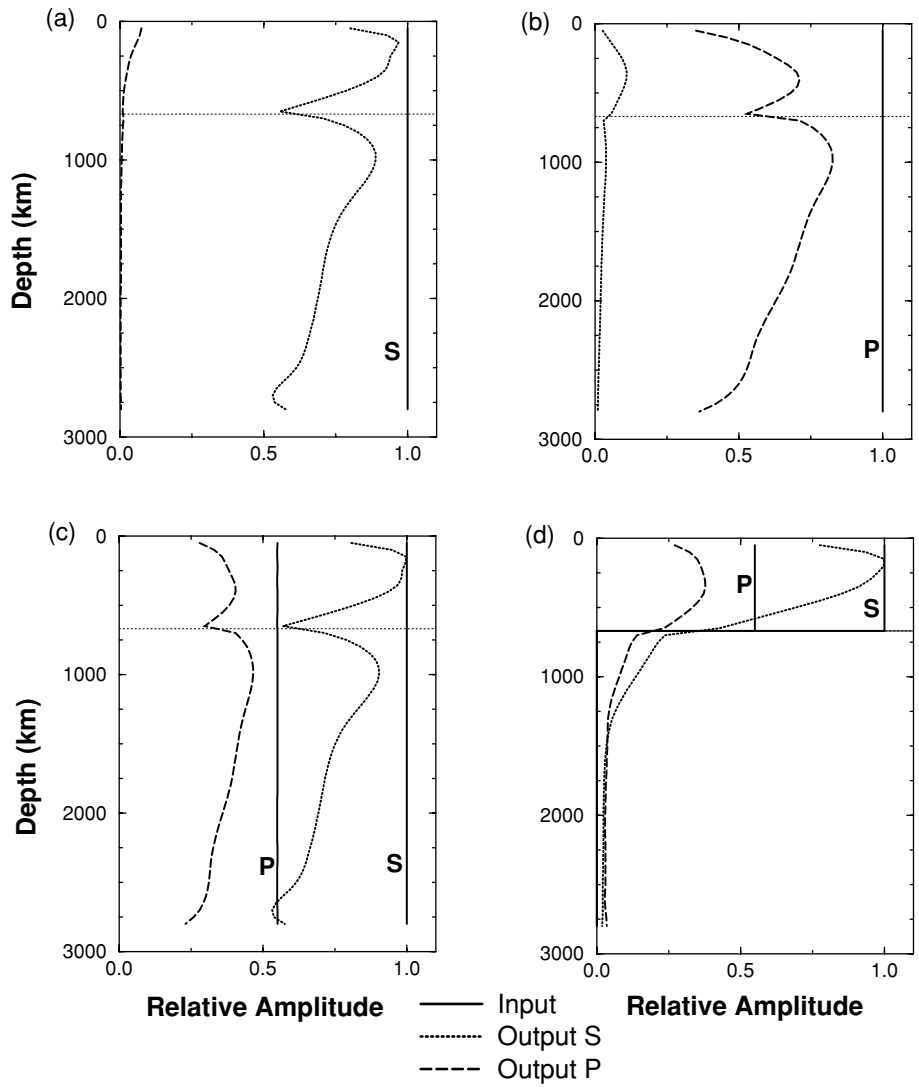

Figure 12. Relative rms amplitude curves of output (normalized by input amplitude) models for the resolution tests. Input models are marked by the solid lines, output *S* velocity models by the dotted curves, and output *P* velocity models by the dashed curves. The horizontal thin dotted line marks position of the 670 km discontinuity. (a) Test 1. (b) Test 2. (c) Test 3. All curves are plotted as rms amplitude relative to the input *S* velocity model. (d) Format similar to (c) but for test 4.

the *P* and *S* models at the top of the lower mantle, corresponding to the minimum between 670 and 1100 km depth that we noted in the real model above. This suggests that this feature is robust. Fig. 13(c) also indicates that the correlation coefficient between bulk sound and shear velocity for the output models is negative both at the top and the bottom of the mantle. Therefore, it suggests that the negative correlation that we observe in those two regions in the real inversion is not resolved. However, we do recover strongly positive correlation in the resolution test in the mid-mantle with the coefficient remaining above 0.5 from 670 km down to 2000 km.

In Fig. 13(d) we show the output value of ν. This ratio is very close to that of the input model (1.8) in the mid-mantle but increases sharply in the upper mantle. Although the amplitudes of both the output *S* and *P* velocity models are below that of the input in the upper mantle, that of the latter is more so, which results in the high anomaly ratio. We attribute this to the much higher sensitivity of the surface waves and waveforms to shear velocity, which results in a tendency for the inversion to avoid fitting the data through perturbations to *P* velocity (this tendency was found to persist even when using vastly different values of the damping coefficients). The same situation occurs at the bottom of the mantle, where it could be rectified somewhat through the use of phases sensitive to D″ structure (such as $P_{\rm diff}$, Kárason & van der Hilst 2001). At present, however, we can only resolve the anomaly ratio in the depth range 670–2700 km.

Fig. 12(d) shows the rms amplitude of the output models for test 4, where we use a chequerboard pattern as input for the upper mantle only. Smearing of anomalies occurs for ∼600 km across the 670 km boundary, especially for *P* velocity. Just below the boundary, the amplitude of these fictitious anomalies is nearly 50 per cent of those recovered in the upper mantle for *P* velocity, while it is only one-quarter of those recovered for *S* velocity. Some leakage of upper-mantle structure into the lower mantle should be expected even though we have used a discontinuous radial parametrization. This would make it very difficult, for example, to resolve abrupt changes in the pattern of heterogeneities in *P* velocity across the 670 km discontinuity similar to those observed by Gu *et al.* (2001) in shear velocity. However, the results of the previous tests show

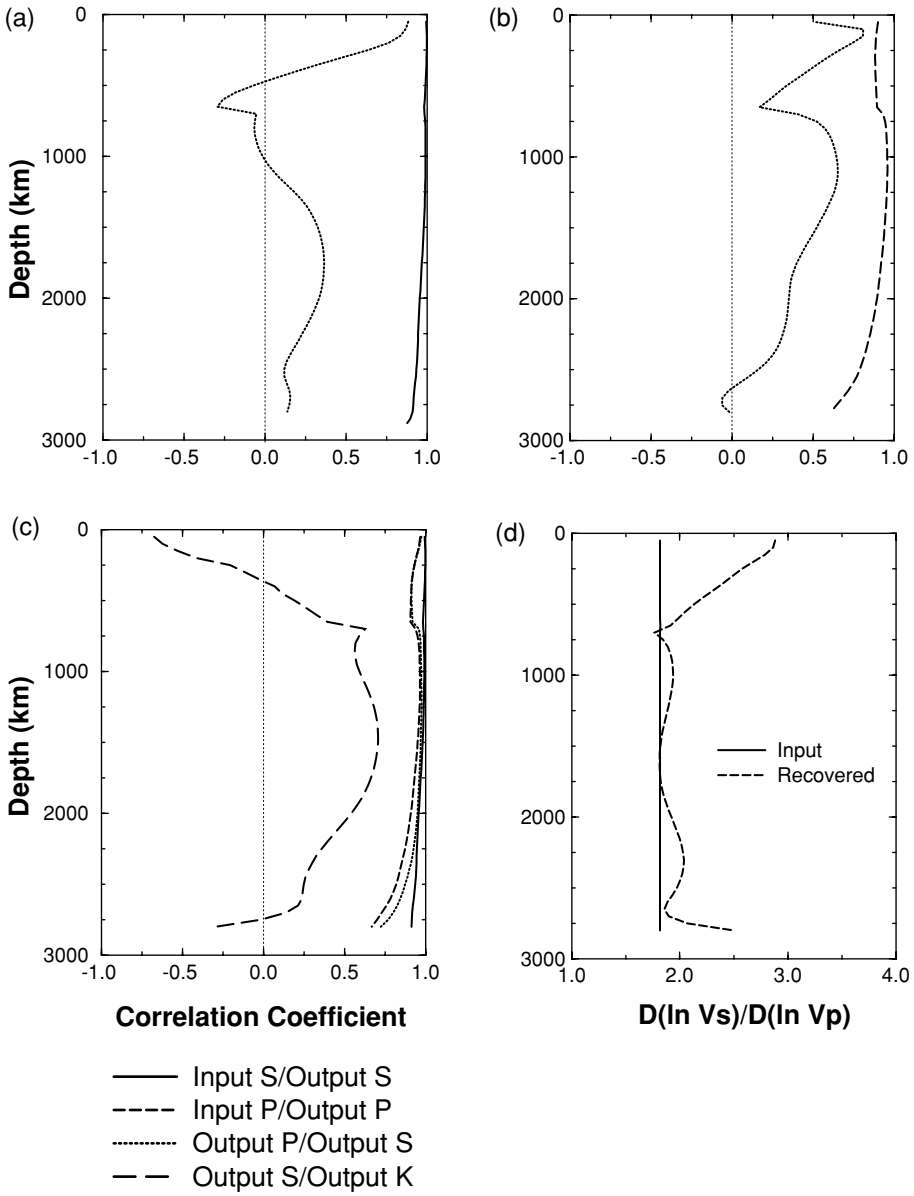

Figure 13. (a) Correlation coefficient versus depth between models for resolution test 1. The solid curve shows correlation between input and output *S* velocity models and the dotted curve shows correlation between recovered *P* and *S* velocity. (b) Correlation between input and output *P* velocity (dashed curve) and between recovered *P* and *S* velocity (dotted curve) for test 2. (c) Correlation between various models for test 3. The long-dashed curve depicts correlation between the recovered *S* velocity model and the bulk sound velocity model computed from the output *S* and *P* velocity perturbations. Other curves are as in (a) and (b). For this test the input *P* and *S* velocity anomalies are perfectly correlated everywhere, as is the shear and bulk-sound velocity anomalies. However, correlation between the recovered shear and bulk sound velocity anomalies is negative above 400 km depth and also at the base of the mantle. (d) Value of ν versus depth for the input and recovered models of test 3. The value is well recovered throughout the lower mantle with the exception of the lowermost 100 km.

that this leakage should not greatly affect the correlation between the recovered models.

5 DISCUSSION AND CONCLUSIONS

5.1 Tests for event location accuracy

As stated in the introduction, improvement in the quality of event locations was one of the motivations for this study. We have used model J362D28 to examine improvement in event location for the explosions and earthquakes used by Antolik *et al.* (2001) and events from the database of the Prototype International Data Centre (pIDC) (Yang & Romney 1999). The latter events were taken from the GT0-5 catalogues (with an assessed location accuracy of 5 km or better). This results in a combined, globally distributed catalogue of 246 test events. We compute locations for each test event using first-arriving *P* phases only in the distance range 25°–96°. For each phase arrival, we compute a traveltime correction for ellipticity, station elevation, the 3-D mantle model (J362D28) and CRUST5.1, assuming the ray path is the same as that in the 1-D reference model (PREM). Fig. 14 shows the rms mislocation distance for the set of test events used by Antolik *et al.* (2001). From left to right in Fig. 14 the four older 3-D models are plotted in order of increasingly fine parametrization. Both SP12 and MK12 are defined laterally by

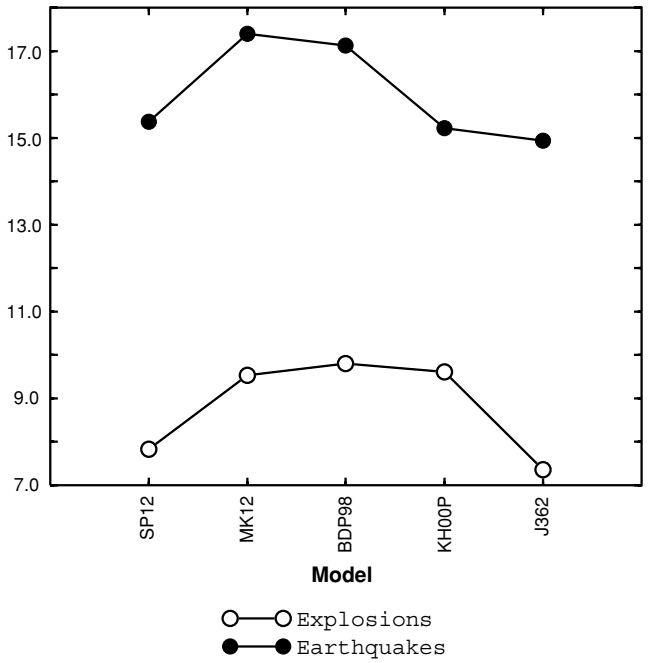

Figure 14. rms mislocation for the reference data set of explosions and earthquakes used by Antolik *et al.* (2001), calculated using five different 3-D models of mantle *P* velocity structure. The location method is described in detail by Antolik *et al.* (2001) and outlined in the text. The five models are, from left to right, SP12WM13 (Su & Dziewonski 1993), MK12WM13 (Su & Dziewonski 1997), BDP98 (Boschi & Dziewonski 1999), KH00P (Kárason & van der Hilst 2001) and J362D28 (present study). The first two models are parametrized by spherical harmonic basis functions up to degree 12, while BDP98 and KH00P are higher-resolution models consisting of constant-velocity blocks.

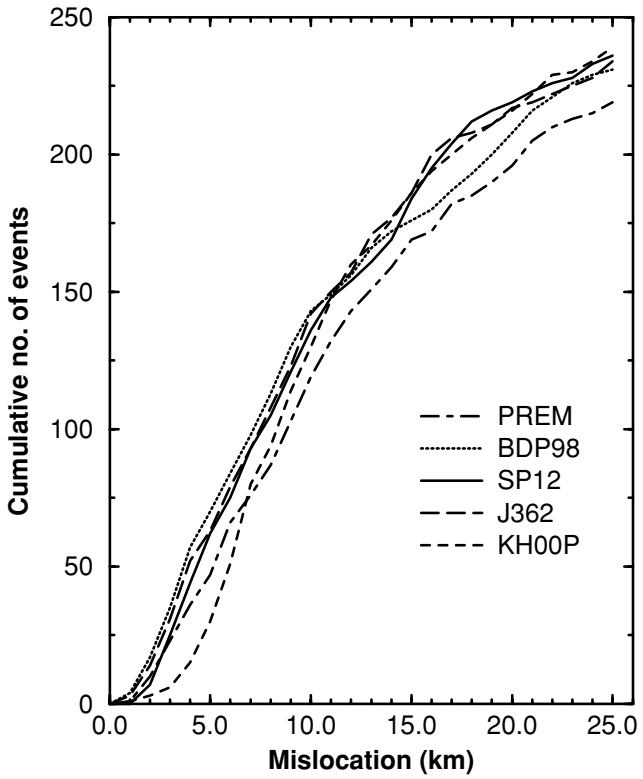

Figure 15. Mislocation statistics for the global reference event database of 246 events. Curves depict the cumulative number of reference events with a mislocation equal to or less than a given value for PREM and four of the models shown in Fig. 15. Models SP12 and J362 give a similar mislocation distribution, but the higher-resolution models show fewer events located with high precision (KH00P) or more events located with lower precision (BDP98).

spherical harmonic functions up to degree 12, while BDP98 and KH00P are block models with dimensions 5° and 3°, respectively. For the explosions, the trend noted by Antolik *et al.* (2001) of increasing location error with resolution of the 3-D model is clearly evident. The exception is for model J362D28, which achieves an improvement of ∼10 per cent in rms mislocation for the explosions over model SP12. J362D28 also improves the origin time error for the explosions by an average of 0.05 s over model SP12. The vast difference in rms location between the explosions and earthquakes overall is probably caused by a suspected greater error in reference location for the earthquakes.

Fig. 15 shows the cumulative distribution of the test events with respect to mislocation distance for four 3-D models and PREM. The difference in location accuracy between the new model and SP12 is small but consistent for all events that have mislocation vectors of less than 15 km. It is interesting to note that for the best located events (with a mislocation of less than 10 km), model BDP98 is actually the best of the 3-D models shown; however, it does not perform nearly as well for events with larger location errors. For events with a mislocation greater than 15 km the curve for BDP98 is closer to PREM than for the other 3-D models. The lower rms mislocation statistic for J362D28 and SP12 is caused by improvement in the fraction of events that is most poorly located. On the other hand, model KH00P performs approximately as well as J362 and SP12 for events with relatively large mislocations but there are fewer events with very small mislocations (<7 km) than for all of the other models including PREM.

In theory, 3-D models with finer parametrization such as BDP98 and KH00P should lead to better velocity resolution in areas with sufficient data sampling. Until recently, however, nearly all global high-resolution models of *P* velocity have been constructed using only seismic traveltimes owing to the high computational demands of such models. However, as Fig. 2 shows, areas in the upper mantle where high data sampling is obtainable is limited mainly to continental regions near large densities of seismic sources or stations. It is therefore quite possible that long-wavelength anomalies having a significant effect on teleseismic traveltime residuals are not as well recovered in such models. For example, Fig. 16 shows traveltime corrections to teleseismic *P* phases for an event located at the Nevada Test Site (NTS) calculated for models BDP98, SP12 and J362D28. The latter two models predict longer-wavelength, generally larger-amplitude traveltime anomalies than does BDP98, although the sign of the corrections agrees in most areas. This pattern is observed for a number of the test event source regions. The lower-resolution velocity models produce much better locations for the NTS explosions. The mislocation vectors are more than 50 per cent smaller in magnitude for model J362D28 than for BDP98.

5.2 *S* to *P* anomaly ratio

The results of our resolution tests indicate that the value of ν is well resolved in most of the lower mantle. This ratio is relatively constant between 2.0 and 2.5, with indication of an increasing trend below a minimum at ∼1700 km depth. This is consistent with estimates of many other models resulting from independent and joint inversions

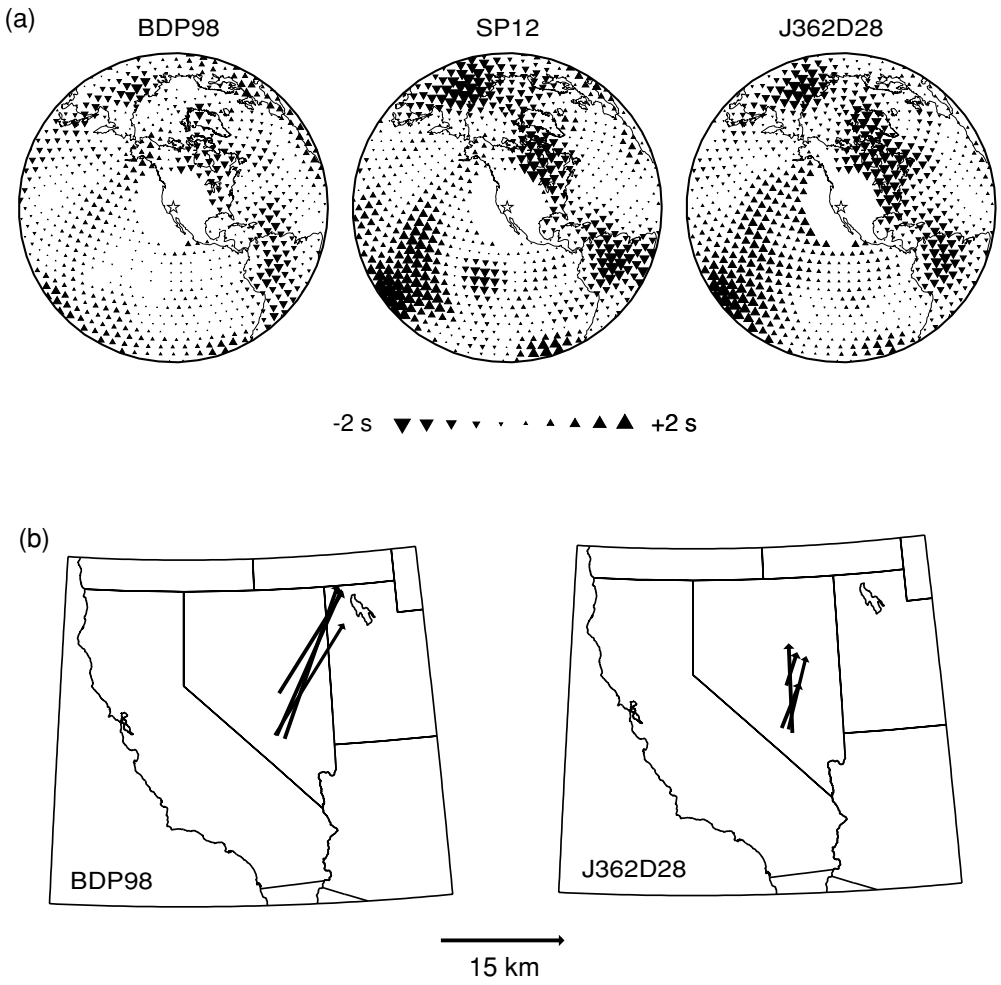

Figure 16. (a) Traveltime corrections to teleseismic *P* waves (relative to PREM) calculated for an event located at the Nevada Test Site for (left) model BDP98, (centre) model SP12 and (right) model J362D28. Each symbol depicts the correction for a hypothetical seismic station located at that position. Note that the corrections using models SP12 and BDP98 are similar, whereas BDP98 predicts corrections that are generally of the same sign but smaller in amplitude. (b) Mislocation vectors for events in the global reference database located at or near NTS. Arrows point in direction of the model-derived location. Scale given at bottom for reference. The left map is for model BDP98 and the right map for J362D28.

(see Fig. 7 and Becker & Boschi 2002). The relevance of determining this ratio using data with sensitivities to different portions of the seismic frequency band is debatable; however, it was suggested by Masters *et al.* (2000) that long- and short-period traveltime residuals show similar patterns. They suggested that the optimal approach for tomography is to combine ISC traveltime residuals for *P* waves with longer-period waveform-derived traveltimes for *S*, as we do here. Interestingly, the model obtained by Ishii & Tromp (2001) using only normal-mode observations shows higher values of this ratio. The lower-mantle value of ν from our model is also consistently lower than that of Su & Dziewonski (1997) despite the fact that we have used a good portion of the same data (Fig. 7). This could be caused by the particular inversion method used by Su & Dziewonski (1997), which attempted to minimize perturbations in the bulk sound velocity relative to those in shear velocity.

Estimates of the value of ν related to purely thermal effects range from 1.7 to 2.1 (Agnon & Bukowinski 1990; Karato 1993; Karato & Karki 2001). In addition, Karato & Karki (2001) estimate that thermal variations alone could cause a ν value as high as 2.7 in the lower mantle if anelastic effects are considered. Therefore, the value that we observe is not necessarily indicative of chemical heterogeneities in the lower mantle. On the other hand, if the increase below 1700 km depth is real, it could indicate increasing effects owing to chemical heterogeneity in this depth range. The increase in ν below 1700 km is largely caused by the increase in the amplitude of the shear velocity heterogeneity (largely in regions of negative velocity perturbations), whereas the rms amplitude of the *P* velocity model remains nearly constant until ∼2000 km depth (Fig. 7). Therefore, it suggests an opposite perturbation in the bulk sound velocities around this depth, which would be consistent with increasing chemical heterogeneity (i.e. the rms amplitude curve for bulk sound velocity perturbations also shows an increase at 1700 km, with a reversal of this trend around 2000 km when the *P* velocity perturbations begin to increase in amplitude more rapidly). It is tempting to attribute the gradient in the anomaly ratio, along with a reorganization in the power spectra at approximately the same depth (Gu *et al.* 2001) to increasing chemical heterogeneity in this portion of the lower mantle (Kellogg *et al.* 1999; van der Hilst & Kárason 1999). In addition, a large gradient in the viscosity profile with depth has been inferred by Forte & Mitrovica (2001) below 1700 km. If this region represents a chemically distinct layer that has not mixed well with the mantle above, then one might expect it to be marked by

a sharp transitional boundary. However, the change in the character of the anomalies in both *P* and *S* velocity is very gradual, and attempts to detect discontinuities in the flow pattern have thus far proven elusive (Gu *et al.* 2001).

It has become increasingly popular to cite the large value of ν (and negative correlation between bulk sound and shear velocity anomalies) in the deep lower mantle (D″ region), observed in a number of previous studies, as evidence for chemical heterogeneity (Robertson & Woodhouse 1996; Ishii & Tromp 1999; Masters *et al.* 2000). However, we must note that the resolution tests show that our ability to resolve the ratio below 2700 km is significantly degraded by the loss of resolution in *P* velocity. Therefore, the value of ν should be interpreted with caution in the D″ region. In fact, the anomaly ratio shows a marked decrease just above the CMB. Because the quantity and quality of data used in this study is at least equal to that used in previous joint inversions, it is unlikely that this situation is markedly different in those previous studies.

There are two features in the anomaly ratio curve in the upper mantle that merit discussion. The first is the peak in the value of ν that is observed in the transition zone. Fig. 7 shows that this peak is caused by an increase in the rms amplitude of the shear velocity model just above the 670 km discontinuity. In the same region, the amplitude of the *P* velocity model is fairly constant or slightly decreasing. It is here that the shear velocity model shows the biggest difference with model S362D1. As mentioned above, the amplitude increase in the transition zone may be the source of the improvement in variance reduction that we achieve to some of the waveform data sets. It is interesting to note that a dramatic increase in rms amplitude was pointed out by Fukao *et al.* (2001) when sampling *P* and *S* velocity models only in the regions of recent subduction where oceanic lithosphere may have ponded in the transition zone. The comparison between *P* and *S* velocity models recently presented by Becker & Boschi (2002) shows several models where the amplitude is constant or increases slightly in the transition zone. Dziewonski & Woodhouse (1987) originally suggested greater shear velocity anomalies at 670 km depth in comparison with those at 500 or 800 km. Because of the lower resolution for *P* velocity in the transition zone that is revealed by the resolution tests, however, we hesitate to interpret the peak in the value of ν observed in the depth range 400–670 km as a real feature.

The second feature is the large peak in the value of ν obtained in the very shallow mantle. This is almost certainly the result of weaker resolution for *P* than *S* velocity. Here the greatest control on the models is the surface wave dispersion measurements. These are approximately an order of magnitude more sensitive to shear velocity variations. This result may not occur if enough regional traveltimes are included in a joint inversion to achieve adequate coverage of the shallow mantle. However, because of the difficulty of predicting the travel paths for rays in the highly heterogeneous shallow mantle and the higher noise level in these data (Gudmundsson *et al.* 1990), we have omitted them from this study. As a result the amplitude of anomalies in the upper 100–200 km are probably underestimated by a factor of around 2 (Fig. 12).

5.3 Pattern of heterogeneities

We noted earlier the drop in correlation between *P* and *S* velocities exhibited by the final model in the depth range 670–1100 km. Two pieces of evidence support this aspect of the model. The first of these is the poor fit provided by the starting 3-D model (scaled S362D1) to the *P*-wave residuals. Fig. 17 shows the correlation between the observed *P*-wave residuals and those predicted by the starting and final models. For the final model, the correlation remains at or above 0.8 for phases turning throughout the lower mantle. However, the residuals predicted by the starting model show a sharp minimum in correlation for rays bottoming just beneath the 670–1100 km range. The fact that the fit to the *P*-wave residuals provided by the starting model is actually worse than PREM (Table 1) also indicates a slight tendency for the starting model to predict anomalies of opposite sign to what are observed.

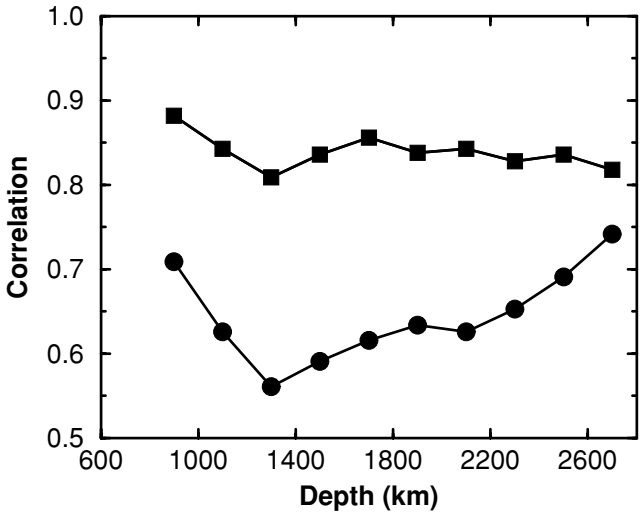

Figure 17. Curves showing the correlation between the residuals for *P* waves predicted by the final model (squares) and the observed *P*-wave residuals, and the correlation between the observed residuals and those predicted by the starting model for the inversion (squares). Each symbol represents the correlation between cap-averaged residuals (radius of 5°) for those *P* waves bottoming in a depth range of 400 km centred on that point. The lower curve (for observed/starting model) shows a distinct minimum in correlation for *P* waves that turn around 1200 km depth.

Secondly, no such broad decorrelation between *P* and *S* velocities was observed in the resolution experiments. We inverted a chequerboard pattern that was perfectly correlated throughout the mantle and obtained a high correlation between the output models between 670 and 1100 km depth (Fig. 13). However, this particular test may represent an ideal case because the input structure above 670 km was perfectly correlated with the structure below. Therefore, we performed another test using the same input chequerboard pattern, but in this case the sign of the anomalies was abruptly reversed at 670 km. Thus the structure above 670 km is perfectly anticorrelated with that below. The output models from this experiment are shown at depths of 550, 650, 750 and 850 km in Fig. 19. Although there is indeed a slight drop in correlation below 670 km, which is the result of the upper-mantle structure bleeding into the top of the lower mantle, the correct anomaly pattern is still very well recovered at a depth of 750 km. The correlation between the output models at this depth has increased almost to the level exhibited just above 670 km.

A lower than usual correlation between shear and compressional anomalies at the top of the lower mantle could indicate greater chemical heterogeneity in this region than deeper in the mantle. Recently, Fukao *et al.* (2001) discussed a tendency for subducted slabs to pile up between 670 and 1000 km depth. They noted that seismic velocity structure above a depth of 1000 km tends to be poorly correlated with that below, and favour 1000 km as the more appropriate depth for the bottom of the transition zone. It is not entirely clear how the accumulation of slab material in the transition region may lead to low correlation between *P* and *S* velocities. In the immediate

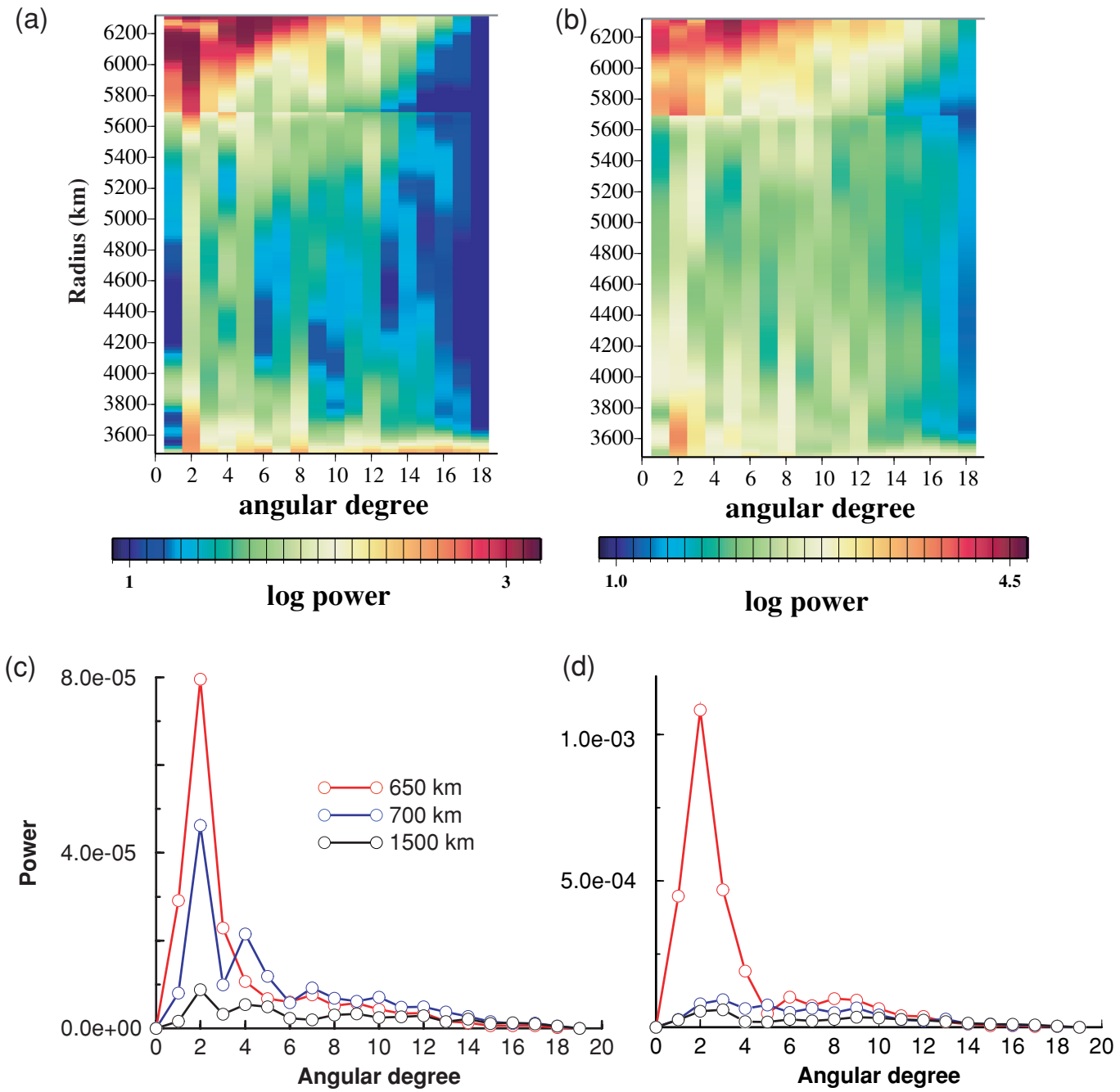

Figure 18. (a) Log power spectra of model J362D28 *P* velocity for spherical harmonic degrees 1–18. (b) Log power spectra for model J362D28 *S* velocity. Note the difference in colour scale from (a). (c) Linear plot of power spectra for *P* velocity at depths of 650, 700 and 1500 km depth. (d) Same as (c) for *S* velocity. The power in degree two does not drop abruptly in amplitude at 670 km for *P* velocity structure as it does for *S* velocity structure. The degree-two power remains the highest for *P* velocity throughout the mantle.

vicinity of subduction zones, the thermal effect should dominate, leading to high correlation between *P* and *S* velocities. However, away from subduction zones where horizontal flow is more prominent, thermal effects should be less important. A pile up of subducted oceanic lithosphere could affect *P* and *S* velocities differently in this depth range. Until recently, most *P*-wave tomography has focused mainly on the vicinity of subduction zones. There are also widespread reports of seismic discontinuities between 800 and 1200 km depth (e.g. Kawakatsu & Niu 1994, 1996; Vinnik *et al.* 1998), which could separate regions of somewhat different chemical composition. Interestingly, 1000 km also corresponds to the approximate depth of an order of magnitude increase in mantle viscosity inferred by Mitrovica & Forte (1997, 2002).

Fig. 18 shows the heterogeneity spectrum up to degree 18 for both *P* and *S* velocity. The shear velocity spectrum (with dominance of low degrees in the upper mantle and D″ region and a white spectrum in the mid-mantle) is similar to that reported in other studies (e.g. Gu *et al.* 2001). The compressional velocity spectrum shows most of these same general features, but with some subtle differences. We do not observe a sharp drop in degree two across

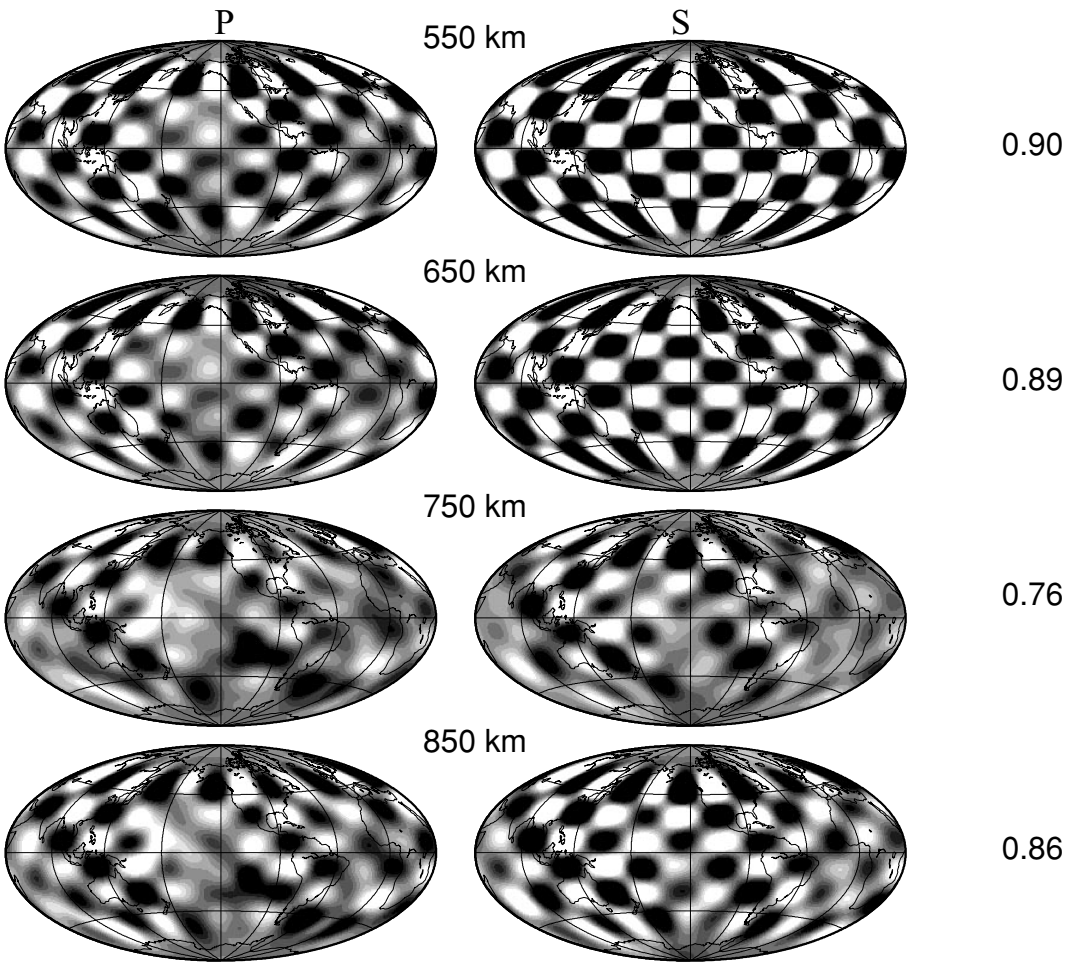

Figure 19. Recovered *P* (left) and *S* velocity (right) models for a chequerboard test at depths of 550, 650, 750 and 850 km. The input structure consists of that shown in Fig. 10, but with the pattern of anomalies reversed in sign between the upper and lower mantle. Numbers shown on the right are the correlation coefficients between *P* and *S* velocity at each of the four depths.

670 km as we observe for shear velocity. Instead the transition to a more white spectrum occurs over a broader depth range of approximately 100 km. This could well be caused by the bleeding of upper-mantle structure into the top of the lower mantle, such as we observe in our resolution experiments. The power in degree two at 700 km, for example, is close to the 50 per cent level (relative to that above 670 km) that we found for test 4. In other words, our results are consistent with a similar reorganization in the anomaly patterns for compressional velocity as was found by Gu *et al.* (2001) for shear velocity, but they do not require this. However, Fig. 18 also shows that even though the spectrum does become whiter at mid-mantle depths, the slight dominance of degrees 2–5 over higher degrees continues down to the CMB. The minimum in power around 2000 km depth for *P* velocity mentioned above is evident in Fig. 18 as opposed to the shallower transition for *S* velocity (∼1700 km). The D″ region contains larger-amplitude short-wavelength structure in *P* velocity (i.e. less dominance of degree two). This may be partially explained by the lower resolution for *P* velocity, and hence greater reduction in amplitude in the D″ region. On the other hand, there have been several recent observations of short-wavelength compressional velocity structure just above the CMB (e.g. Bréger *et al.* 2000; Tkalčić *et al.* 2002). Our *P* velocity model at ∼2800 km (Fig. 6), despite the fact that the resolution tests indicate degrading resolution above the CMB, is quite similar in structure and amplitude to the models published by Tkalčić *et al.* (2002) derived from *PKP* differential traveltimes. In agreement with those authors' study, our model shows fast velocities under central America, east Asia and across the N. Pacific (although the latter is somewhat narrower in the present study). Slow-velocity anomalies also exist in the southwest Pacific, under Africa and under western North America in both models. The primary difference is that we do not see the large slow anomaly under South America. Instead our model shows fast velocities. However, the resolution experiments indicate that our resolution is poor beneath South America at the base of the mantle (Fig. 11).

5.4 Conclusions

We have performed a joint inversion for *P* and *S* velocity anomalies using a radial and horizontal spline parametrization. This parametrization carries the dual advantage of a local basis combined with the production of a smoothly varying model. As a result, portions of the model can readily be replaced with more detailed, regional models (e.g. Boschi 2001). We use a large suite of data combining both absolute and differential traveltimes, complete waveforms and surface wave phase velocity measurements. There are two principal conclusions from this study. In most of the lower mantle, where we are able to resolve the amplitude ratio

between compressional and shear velocity anomalies, this ratio ranges between 2.0 and 2.5. We also observe a minimum in correlation between *P* and *S* velocity in the depth range 670–1100 km, and the bulk-sound velocity is negatively correlated with shear velocity throughout the lower mantle.

We have tested the ability of our *P* velocity model to produce accurate locations for seismic events. One of the objectives of this study is to reverse the trend found by Antolik *et al.* (2001) of little improvement in event locations with increasing resolution of the 3-D velocity model employed. This objective appears to be met, as we are able to reduce the rms mislocation for explosions by approximately 10 per cent over the best model tested by those authors. The results of the relocation tests indicate that model J362D28 is capable of producing accurate teleseismic station corrections for calibration of the IMS seismic network and monitoring of the CTBT.

ACKNOWLEDGMENTS

The authors wish to thank L. Boschi, H. Tkalčić, J. X. Mitrovica and W. Hamilton for interesting discussions. L. Boschi performed the inversion depicted in Fig. 3. J. Ritsema and an anonymous reviewer provided helpful reviews of the manuscript. G. Laske provided the data set of *PP–P* traveltimes. The figures were produced using Generic Mapping Tools (GMT) and XMgr software.

REFERENCES

Agnon, A. & Bukowinski, M., 1990. δ_s at high pressure and $d \ln v_s / d \ln v_p$ in the lower mantle, *Geophys. Res. Lett.,* **17,** 1149–1152.

Antolik, M., Ekström, G. & Dziewonski, A.M., 2001. Global event location with full and sparse datasets using three-dimensional models of mantle, *P* wave velocity, *Pure appl. Geophys.,* **158,** 291–317.

Becker, T.W. & Boschi, L., 2002. A comparison of tomographic and geodynamic mantle models, *Geophys. Geochem. Geosyst.,* **3,** 10.1029/2001GC000 168.

Boschi, L., 2001. Applications of linear inverse theory in modern global seismology, *PhD thesis,* Harvard Univ., Cambridge, MA, p. 198.

Boschi, L. & Dziewonski, A.M., 1999. 'High' and 'low' resolution images of the Earth's mantle: implications of different approaches to tomographic modeling, *J. geophys. Res.,* **104,** 25 567–25 594.

Bréger, L., Tkalčić, H. & Romanowicz, B., 2000. The effect of D″ on PKP(AB–DF) travel time residuals and possible implications for inner core structure, *Earth planet. Sci. Lett.,* **175,** 133–143.

Chiao, L.-Y. & Kuo, B.-Y., 2001. Multiscale seismic tomography, *Geophys. J. Int.,* **145,** 517–527.

Dziewonski, A.M. & Anderson, D.L., 1981. Preliminary reference Earth model, *Phys. Earth planet. Inter.,* **25,** 297–356.

Dziewonski, A.M. & Woodhouse, J.H., 1987. Global images of the Earth's interior, *Science,* **236,** 37–48.

Ekström, G. & Dziewonski, A.M., 1998. The unique anisotropy of the Pacific upper mantle, *Nature,* **394,** 168–172.

Ekström, G., Tromp, J. & Larson, E.W.F., 1997. Measurements and global models of surface wave propagation, *J. geophys. Res.,* **102,** 8137–8157.

Engdahl, E.R., van der Hilst, R.D. & Buland, R.P., 1998. Global teleseismic earthquake relocation with improved travel times and procedures for depth determination, *Bull. seism. Soc. Am.,* **88,** 722–743.

Firbas, P., 2000. Location calibration based on 3-D modelling, in *Advances in Seismic Event Location, Modern Approaches in Geophysics,* Vol. 18, pp. 135–161, eds Thurber, C.H. & Rabinowitz, N., Kluwer, Dordrecht.

Forte, A.M. & Mitrovica, J.X., 2001. Deep-mantle high-viscosity flow and thermochemical structure inferred from seismic and geodynamic data, *Nature,* **410,** 1049–1056.

Forte, A.M. & Woodward, R.L., 1997. Seismic-geodynamic constraints on three-dimensional structure, vertical flow, and heat transfer in the mantle, *J. geophys. Res.,* **102,** 17 981–17 994.

Fukao, Y., Widiyantoro, S. & Obayashi, M., 2001. Stagnant slabs in the upper and lower mantle transition region, *Rev. Geophys.,* **39,** 291–323.

Grand, S.P., van der Hilst, R.D. & Widiyantoro, S., 1997. Global seismic tomography: a snapshot of convection in the Earth, *GSA Today,* **7,** 1–7.

Group-2 Calibration Consortium, 2000. Source specific station corrections for International Monitoring System seismic stations in North Africa, the Middle East, and western Asia, in *Proc. 22nd Ann. DoD/DOE Seismic Research Symp., Planning for Verification and Compliance with the Comprehensive Nuclear-Test-Ban Treaty,* pp. 359–368, New Orleans, LA.

Gu, Y.J., Dziewonski, A.M., Su, W. & Ekström, G., 2001. Models of mantle shear velocity and discontinuities in the pattern of lateral heterogeneities, *J. geophys. Res.,* **106,** 11 169–11 199.

Gudmundsson, O., Davis, J.H. & Clayton, R.W., 1990. Stochastic analysis of global travel time data: mantle heterogeneity and random errors in the ISC data, *Geophys. J. Int.,* **102,** 25–43.

Ishii, M. & Tromp, J., 1999. Normal-mode and free-air gravity constraints on lateral variations in velocity and density of Earth's mantle, *Science,* **285,** 1231–1236.

Ishii, M. & Tromp, J., 2001. Even-degree lateral variations in the Earth's mantle constrained by free oscillations and the free-air gravity anomaly, *Geophys. J. Int.,* **145,** 77–96.

Kárason, H. & van der Hilst, R.D., 2001. Tomographic imaging of the lowermost mantle with differential times of refracted and diffracted core phases (*PKP*, P_{diff}), *J. geophys. Res.,* **106,** 6569–6587.

Karato, S., 1993. Importance of anelasticity in the interpretation of seismic tomography, *Geophys. Res. Lett.,* **20,** 1623–1626.

Karato, S. & Karki, B., 2001. Origin of lateral variation of seismic wave velocities and density in the deep mantle, *J. geophys. Res.,* **106,** 21 771–21 783.

Kawakatsu, H. & Niu, F., 1994. Seismic evidence for a 920-km discontinuity in the mantle, *Nature,* **371,** 301–305.

Kawakatsu, H. & Niu, F., 1996. Depth variation of the '920-km discontinuity' in the mid-mantle, *Ann. Geofis.,* **14,** 1–43.

Kellogg, L.H., Hager, B.H. & van der Hilst, R.D., 1999. Compositional stratification in the deep mantle, *Science,* **283,** 1881–1884.

Kennett, B.L.N., Widiyantoro, S. & van der Hilst, R.D., 1998. Joint seismic tomography for bulk sound and shear wave speed in the Earth's mantle, *J. geophys. Res.,* **103,** 12 469–12 493.

Liu, X.-F. & Dziewonski, A.M., 1998. Global analysis of shear wave velocity anomalies in the lowermost mantle, in *Core–Mantle Boundary, Geophys. Monograph Ser.,* Vol. 28, pp. 21–36, ed. Gurnis, M., AGU, Washington, DC.

Masters, G., Laske, G., Bolton, H. & Dziewonski, A., 2000. The relative behavior of shear velocity, bulk sound speed, and compressional velocity in the mantle: implications for chemical and thermal structure, in *Earth's Deep Interior: Mineral Physics and Tomography From the Atomic to the GLobal Scale, Geophys. Monograph Ser.,* Vol. 117, pp. 63–87, eds Karato, S. *et al.*, AGU, Washington, DC.

Mitrovica, J.X. & Forte, A.M., 1997. Radial profile of mantle viscosity: results from the joint inversion of convection and postglacial rebound variables, *J. geophys. Res.,* **102,** 2751–2769.

Mitrovica, J.X. & Forte, A.M., 2002. On the radial profile of mantle viscosity, to be published in *Ice Sheets, Sea Level and the Dynamic Earth*, eds Mitrovica, J.X. & Vermeersen, L.L.A., AGU Geodyn. Ser. Vol. 29, American Geophysical Union, Washington, DC.

Mooney, W., Laske, G. & Masters, G., 1998. Crust 5.1: a new global crustal model at 5 × 5 degrees, *J. geophys. Res.,* **103,** 727–747.

Nettles, M., Peccei, C., Ekström, G. & Dziewonski, A.M., 2000. Measurements and models of very long period surface wave propagation, *EOS, Trans. Am. geophys. Un.,* **81,** F822–F823.

Ritsema, J. & van Heijst, H.-J., 2002. Constraints on the correlation of *P*- and *S*-wave velocity heterogeneity in the mantle from *P*, *PP*, *PPP* and PKP_{ab} traveltimes, *Geophys. J. Int.,* **149,** 482–489.

Robertson, G.S. & Woodhouse, J.H., 1995. Evidence for proportionality of *P* and *S* heterogeneity in the lower mantle, *Geophys. J. Int.,* **123,** 85–116.

Robertson, G.S. & Woodhouse, J.H., 1996. Ratio of relative *S* to, *P* velocity heterogeneity in the lower mantle, *J. geophys. Res.,* **101,** 20 041–20 052.

Ryaboy, V., Baumgardt, D.R., Firbas, P. & Dainty, A.M., 2001. Application of 3-D crustal and upper mantle velocity model of North America for location of regional seismic events, *Pure appl. Geophys.,* **158,** 79–103.

Smith, G.P. & Ekström, G., 1996. Improving teleseismic event locations using a three-dimensional earth model, *Bull. seism. Soc. Am.,* **86,** 788–796.

Su, W. & Dziewonski, A.M., 1993. Joint 3-D inversion for *P*- and *S*-velocity in the mantle, *EOS, Trans. Am. geophys. Un.,* **74,** 557.

Su, W. & Dziewonski, A.M., 1997. Simultaneous inversion for 3-D variations in shear and bulk velocity in the mantle, *Phys. Earth planet. Inter.,* **100,** 135–156.

Su, W., Woodward, R.L. & Dziewonski, A.M., 1994. Degree-12 model of shear velocity heterogeneity in the mantle, *J. geophys. Res.,* **99,** 6945–6980.

Tkalčić, H., Romanowicz, B. & Huoy, N., 2002. Constraints on D″ structure using PKP(AB–DF), PKP(BC–DF), and PcP–P travel time data from broadband records, *Geophys. J. Int.,* **148,** 599–616.

Trefethen, L.N. & Bau, D., 1997. *Numerical Linear Algebra,* SIAM, Philadelphia.

van der Hilst, R. & Kárason, H., 1999. Compositional heterogeneity in the bottom 1000 kilometers of Earth's mantle: toward a hybrid convection model, *Science,* **283,** 1885–1888.

van der Voo, R., Spakman, W. & Bijwaard, H., 1999. Mesozoic subducted slab under Siberia, *Nature,* **397,** 246–249.

Vasco, D.W. & Johnson, L.R., 1998. Whole Earth structure estimated from seismic arrival times, *J. geophys. Res.,* **103,** 2633–2671.

Vinnik, L., Niu, F. & Kawakatsu, H., 1998. Broadband converted phases from midmantle discontinuities, *Earth Planets Space,* **50,** 987–997.

Wang, Z. & Dahlen, F., 1995. Spherical-spline parameterization of three-dimensional Earth models, *Geophys. Res. Lett.,* **22,** 3099–3102.

Woodhouse, J.H. & Dziewonski, A.M., 1984. Mapping the upper mantle: three-dimensional modeling of earth structure by inversion of seismic waveforms, *J. geophys. Res.,* **89,** 5953–5986.

Woodhouse, J.H. & Dziewonski, A.M., 1989. Seismic modeling of the Earth's large-scale three-dimensional structure, *Phil. Trans. R. Soc. Lond.,* A., **328,** 291–308.

Yang, X. & Romney, C., 1999. pIDC ground truth database, Center for Monitoring Research publication, CMR-99/15, p. 120.

Zhou, L., Jordan, T.H. & Chapman, C.H., 2000. Three-dimensional Frèchet differential kernels for the seismic delay times, *Geophys. J. Int.,* **141,** 558–576.